Modeling and Parametric Simulations of Solid Oxide Fuel Cells with Methane Carbon Dioxide Reforming

Meng Ni*

Building Energy Research Group, Department of Building and Real Estate

The Hong Kong Polytechnic University, Hung Hom, Kowloon, Hong Kong, China

Abstract:

A two-dimensional model is developed to simulate the performance of solid oxide fuel cells (SOFCs) fed with CO_2 and CH_4 mixture. The electrochemical oxidations of both CO and H_2 are included. Important chemical reactions are considered in the model, including methane carbon dioxide reforming (MCDR), reversible water gas shift reaction (WGSR), and methane steam reforming (MSR). It's found that at a CH_4/CO_2 molar ratio of 50/50, MCDR and reversible WGSR significantly influence the cell performance while MSR is negligibly small. The performance of SOFC fed with CO_2/CH_4 mixture is comparable to SOFC running on CH_4/H_2O mixtures. The electric output of SOFC can be enhanced by operating the cell at a low operating potential or at a high temperature. In addition, the development of anode catalyst with high activity towards CO electrochemical oxidation is important for SOFC performance enhancement. The model can serve as a useful tool for optimization of the SOFC system running on CH_4/CO_2 mixtures.

Keywords: Solid oxide fuel cell; Hydrocarbon fuels; Methane carbon dioxide reforming; Electrochemistry; Porous media; Heat and mass transfer

---

* Corresponding author. Tel: (852) 2766 4152; Fax: (852) 2764 5131;
Email: bsmengni@polyu.edu.hk (Meng Ni)

1. Introduction

Solid oxide fuel cells (SOFCs) are very promising electrochemical devices for stationary power generation [1]. Working at a high temperature (i.e. 673-1273K), SOFCs have a few advantages: (1) use of low cost catalyst (i.e. Ni as anode) due to fast electrochemical reaction rate; (2) relatively low activation loss compared with low temperature fuel cells; (3) potential for combined heat and power (CHP) cogeneration as the waste heat from the SOFC stack is of high quality and can be recovered; (4) fuel flexibility – high working temperature enables direct internal reforming of hydrocarbon fuels or thermal decomposition of ammonia, thus SOFCs can make use of alternative fuels, including hydrogen, methane, coal gas, bio-ethanol, ammonia, dimethyl ether (DME), and other hydrocarbon fuels [2-7]. The fuel flexibility feature makes SOFCs unique compared with low temperature fuel cells, such as proton exchange membrane fuel cells (PEMFCs), which require very pure hydrogen as fuel [8].

Methane is a widely studied fuel for SOFCs as it's the major component of natural gas and a key component of towngas and biogas. For CH_4 fed SOFCs, steam reforming of CH_4 is needed as the direct electrochemical oxidation of CH_4 in SOFCs is still very difficult [9,10]. Extensive experimental and modeling studies have been performed to understand the methane internal steam reforming (MSR) and water gas shift reaction (WGSR) kinetics in SOFCs and their effects on SOFC performance [11-23]. For describing the reaction kinetics of MSR and WGSR, global reaction schemes are widely used due to their easy implementation and less computational time [11-17]. Detailed elementary reaction schemes are also employed for internal reforming SOFCs [18-23]. These studies showed that the inclusion of SR and WGSR greatly influences the transport process and electrochemical performance of the cell. In addition to MSR, methane carbon dioxide reforming (MCDR) has also demonstrated to be feasible for SOFCs [24]. However, there is still no systematic modeling on SOFCs with MCDR. It's still unclear on whether the performance of SOFC with MCDR is comparable to that of SOFC with

MSR. It is also not fully understood on how the inclusion of MCDR can affect the SOFC performance and how to improve the SOFC performance by adjusting the operating conditions. In this study, a 2D numerical model is developed to characterize the transport and reaction phenomena in SOFCs with CO_2/CH_4 mixture as a fuel. The effects of various operating parameters on the cell performance are investigated.

2. Model Development

The working principles and computational domain for SOFCs with CO_2 reforming of CH_4 are shown in Figure 1. Consistent with the previous studies on SOFC with MSR [17,25], the computational domain in the present study contains the interconnector, anode gas channel, porous anode layer, dense electrolyte, porous cathode layer and the air channel. In operation, CO_2/CH_4 gas mixture with a molar ratio of 1:1 is supplied to the anode gas channel and air is supplied to the cathode gas channel. In the porous anode layer, MCDR takes place for CO and H_2 production (Eq. 1). As H_2O is produced from the electrochemical reaction, MSR (Eq. 2) and WGSR (Eq. 3) can also occur.

$$CO_2 + CH_4 \leftrightarrow 2CO + 2H_2 \tag{1}$$

$$CH_4 + H_2O \leftrightarrow CO + 3H_2 \tag{2}$$

$$CO + H_2O \leftrightarrow CO_2 + H_2 \tag{3}$$

The produced H_2 molecules are diffused to the triple-phase-boundary (TPB) at the anode-electrolyte interface, where they react with oxygen ions (O^{2-}) to produce H_2O and electrons (Eq. 4). The electrons flow from the anode to the cathode via an external circuit to produce useful electrical power. At the cathode, O_2 molecules are diffused to the TPB at the cathode-electrolyte interface, where they react with electrons to form oxygen ions (Eq. 5).

$$\mathrm{H_2} + \mathrm{O^{2-}} \rightarrow \mathrm{H_2O} + 2e^- \tag{4}$$

$$0.5O_2 + 2e^- \rightarrow O^{2-} \quad (5)$$

The electrochemical oxidation of CH_4 is neglected due to its relatively low reaction kinetics [26,27]. However, the rate of electrochemical oxidation of CO (Eq. 6) is on the same of order with H_2 fuel and thus it's considered in the present study.

$$CO + O^{2-} \rightarrow CO_2 + 2e^- \quad (6)$$

It should be noted that in addition to reactions (1-3), CH_4 pyrolysis ($CH_4 \leftrightarrow C + 2H_2$) and Boudouard reaction ($2CO \leftrightarrow C + CO_2$) can also occur in the porous anode. The produced carbon may also contribute to power generation due to the two reactions: $C + O^{2-} \rightarrow CO + 2e^-$ and $C + 2O^{2-} \rightarrow CO_2 + 4e^-$. However, in the present study, only reactions (1-6) are considered due to their relatively high reaction rate. In the future studies, the CH_4 pyrolysis and Boudouard reactions can be considered for predicting the carbon deposition kinetics and the SOFC life-time.

Based on the working principles, a 2D thermo-electrochemical model is developed to simulate the coupled transport and reaction phenomena in SOFC. The 2D model consists of 3 sub-models: (1) an electrochemical model; (2) a chemical model; and (3) a computational fluid dynamics (CFD) model.

2.1. Electrochemical model

The electrochemical model is used to calculate the local electrochemical reaction rates (current density *J*: $A.m^{-2}$) at given operating potentials (V). Although the SOFC only exhibits one open-circuit voltage (OCV, or equilibrium potential), it's actually an "average" of the Nernst potentials for H_2 fuel and CO fuel [28]. In the present study, the Nernst potentials for H_2 and CO fuels are calculated separately using their respective gas partial pressures [25,29,30]. In operation, the potential V can be calculated as the equilibrium potential (E, determined from Gibbs free energy change of the reactions [25]) subtracted by all overpotential losses [25,29,30].

$$V = E - \eta_{act,a} - \eta_{act,c} - \eta_{ohmic} \tag{7}$$

$$E_{H_2} = 1.253 - 0.00024516T + \frac{RT}{2F}\ln\left[\frac{P_{H_2}^I \left(P_{O_2}^I\right)^{0.5}}{P_{H_2O}^I}\right] \tag{8}$$

$$E_{CO} = 1.46713 - 0.0004527T + \frac{RT}{2F}\ln\left[\frac{P_{CO}^I \left(P_{O_2}^I\right)^{0.5}}{P_{CO_2}^I}\right] \tag{9}$$

where T is temperature (K). R is the ideal gas constant (8.3145 J.mol^{-1}K^{-1}). F is the Faraday constant (96485 C.mol^{-1}). P^I used for calculating the equilibrium potential for H_2 fuel (Eq. 8) and CO fuel (Eq. 9) denotes the gas partial pressure. It should be mentioned that the partial pressures at the electrode-electrolyte interface are used in Eqs. 8 and 9, thus the concentration overpotentials are included in the Nernst equation calculation. η_{ohmic} is the ohmic overpotential and can be determined with the Ohm's law (Eq. 10).

$$\eta_{ohmic} = JL\frac{1}{\sigma} \tag{10}$$

where L (m) and σ ($\Omega^{-1}.m^{-1}$) are the thickness and ionic conductivity of the electrolyte respectively. J is the current density (Am^{-2}). For YSZ electrolyte, the ionic conductivity can be determined as $\sigma = 3.34\times10^4 \exp\left(-\frac{10300}{T}\right)$ [13].

The activation overpotential related to the H_2 fuel and CO fuel can be calculated as [29,30],

$$\eta_{act,H_2,i} = \frac{RTJ_{H_2}}{n_{H_2}FJ_{H_2,i}^0} \tag{11}$$

$$\eta_{act,CO,i} = \frac{RTJ_{CO}}{n_{CO}FJ_{CO,i}^0} \tag{12}$$

where $J_{H_2,i}^0$ and $J_{CO,i}^0$ (A.m^{-2}) are the exchange current densities for H_2 (Eq. 4) and CO (Eq. 6), respectively. The subscript i (i = a and c) denotes the anode and cathode. J_{H_2} and J_{CO} are

current densities (A.m^{-2}) generated from electrochemical oxidation of H_2 fuel and CO fuel, respectively. By incorporating Eqs. 10-12 into Eq. 7, we can obtain the relationship between the operating potential and the current density, for example, the current density due to H_2 fuel: $V = E_{H_2} - \frac{RTJ_{H_2}}{n_{H_2}FJ^0_{H_2,a}} - \frac{RTJ_{H_2}}{n_{H_2}FJ^0_{H_2,c}} - J_{H_2}L\frac{1}{\sigma}$. Thus the current density (J_{H_2} as an example) can be determined as

$$J_{H_2} = \frac{E_{H_2} - V}{\frac{RT}{n_{H_2}FJ^0_{H_2,a}} + \frac{RT}{n_{H_2}FJ^0_{H_2,c}} + L\frac{1}{\sigma}} \tag{13}$$

To determine J_{H_2}, the chemical model and CFD model must be solved, as the partial pressures of gas species at the electrode-electrolyte interface are used for calculating E_{H_2} (Eq. 8). The values of $J^0_{H_2,a}$ and $J^0_{H_2,c}$ at 1073K are 5300 A.m^{-2} and 2000 A.m^{-2} respectively [31]. From experimental investigations, the electrochemical oxidation rate of H_2 is about 1.9-2.3 times and 2.3-3.1 times that of CO fuel at 1023K and 1073K, respectively [26]. In the present study, $J^0_{CO,a}$ is assumed to be $J^0_{CO,a} = 0.3J^0_{H_2,a}$ for the base case. However, due to limited data on exchange current density for CO fuel [26,28], the chosen data may not be representative. Considering that researchers are developing catalyst to enhance the electrode activity toward CO fuel, $J^0_{CO,a} = 0.6J^0_{H_2,a}$ is also used in the parametric simulation.

2. 2. Chemical model

The chemical model is used to calculate the reaction rates and reaction heat of the chemical reactions in the porous catalyst layer. The reaction rates in the fuel channel are assumed to be negligible due to the lack of catalyst. According to Haberman and Young [11], the reaction rates for MSR (R_{DIR}, mol.m^{-3}.s^{-1}) and WGSR (R_{WGSR}, mol.m^{-3}.s^{-1}) can be calculated below (Eqs. 14-20).

$$R_{WGSR} = k_{sf}\left(p_{H_2O}p_{CO} - \frac{p_{H_2}p_{CO_2}}{K_{ps}} \right) \tag{14}$$

$$k_{sf} = 0.0171\exp\left(\frac{-103191}{RT}\right) \qquad (mol.m^{-3}.Pa^{-2}.s^{-1}) \tag{15}$$

$$K_{ps} = \exp\left(-0.2935Z^3 + 0.6351Z^2 + 4.1788Z + 0.3169\right) \tag{16}$$

$$Z = \frac{1000}{T(K)} - 1 \tag{17}$$

$$R_{MSR} = k_{rf}\left(P_{CH_4}P_{H_2O} - \frac{P_{CO}\left(P_{H_2}\right)^3}{K_{pr}} \right) \tag{18}$$

$$k_{rf} = 2395\exp\left(\frac{-231266}{RT}\right) \tag{19}$$

$$K_{pr} = 1.0267\times10^{10}\times\exp\left(-0.2513Z^4 + 0.3665Z^3 + 0.5810Z^2 - 27.134Z + 3.277\right) \tag{20}$$

The reaction rates for MCDR have been studied by a few groups [24,32,33]. According to Langmuir-Hinshelwood (LH) model, the reaction rate of CO_2 reforming of CH_4 (R_{MCDR}, mol.m^{-3}.s^{-1}) can be written as [32],

$$R_{MCDR} = \frac{k_{co_2}K_{CO_2}K_{CH_4}P_{CO_2}P_{CH_4}}{(1 + K_{CO_2}P_{CO_2} + K_{CH_4}P_{CH_4})^2} \tag{21}$$

$$k_{CO_2} = 1.17\times10^7\exp\left(-\frac{83,498}{RT}\right), \quad \left(mol\cdot m^{-3}\cdot s^{-1}\right) \tag{22}$$

$$K_{CO_2} = 3.11\times10^{-3}\exp\left(\frac{49,220}{RT}\right), \quad atm^{-1} \tag{23}$$

$$K_{CH_4} = 0.653\exp\left(\frac{16,054}{RT}\right), \quad atm^{-1} \tag{24}$$

The reaction heat associated with MSR, WGSR and MCDR can be determined from the enthalpy changes of the three reactions. The heat generation from exothermic WGSR (H_{WGSR},

J.mol^{-1}) and heat consumption by endothermic MSR reaction (H_{MSR}, J.mol^{-1}) can be determined as [34].

$$H_{MSR} = -\left(206205.5 + 19.5175T\right) \tag{25}$$

$$H_{WGSR} = 45063 - 10.28T \tag{26}$$

For endothermic MCDR, the reaction heat is about 256.8kJ.mol^{-1} at 600K and 260.05kJ.mol^{-1} at 1200K [34]. Assuming linear variation with temperature, the reaction heat (consumption) of MCDR (H_{MCDR}, J.mol^{-1}) can be written as

$$H_{MCDR} = -\left(253550.0 + 5.41667T\right) \tag{27}$$

2. 3. Computational fluid dynamic (CFD) model

The CFD model is used to simulate the transport of heat and mass in SOFCs. The gas transport in SOFCs channels is assumed to be laminar as the Reynolds number is low. Recent heat transfer analyses confirm that the local thermal non-equilibrium effect in the SOFC electrodes is negligible [35,36]. Thus the temperatures of the solid and gas in the porous electrodes are assumed to be locally the same (local thermal equilibrium assumption). As a result, only one energy equation is needed. Heat radiation effect is assumed to be small. All gaseous reactants and products are assumed to be ideal gases. The cell is assumed to be in a large SOFC stack, thus the periodic thermal boundary conditions are assumed. That is, the heat fluxes at y = 0 and $y = y_M$ are set to be 0. The governing equations for the CFD model include the conservation laws of mass, momentum, energy and species. The general transport equation can be written as [37],

$$\frac{\partial\left(\rho\phi\right)}{\partial t} + \nabla\left(\rho\mathbf{V}\phi\right) = \nabla\left(\Gamma\nabla\phi\right) + S \tag{28}$$

Here ϕ is a general variable to be solved, which can be 1 (continuity equation, Eq. 29), V (momentum equation, Eqs. 30 and 31), T (energy equation, Eq. 32), and Y_j (mass fraction, for species equation: Eq. 33). t is time. ρ is density. **V** is the velocity vector. Γ is the general diffusion coefficient. S is the general source term.

$$\frac{\partial(\rho U)}{\partial x}+\frac{\partial(\rho V)}{\partial y}=S_m \tag{29}$$

$$\frac{\partial(\rho UU)}{\partial x}+\frac{\partial(\rho VU)}{\partial y}=-\frac{\partial P}{\partial x}+\frac{\partial}{\partial x}\left(\mu\frac{\partial U}{\partial x}\right)+\frac{\partial}{\partial y}\left(\mu\frac{\partial U}{\partial y}\right)+S_x \tag{30}$$

$$\frac{\partial(\rho UV)}{\partial x}+\frac{\partial(\rho VV)}{\partial y}=-\frac{\partial P}{\partial y}+\frac{\partial}{\partial x}\left(\mu\frac{\partial V}{\partial x}\right)+\frac{\partial}{\partial y}\left(\mu\frac{\partial V}{\partial y}\right)+S_y \tag{31}$$

$$\frac{\partial(\rho c_{P,eff}UT)}{\partial x}+\frac{\partial(\rho c_{P,eff}VT)}{\partial y}=\frac{\partial}{\partial x}\left(k_{eff}\frac{\partial T}{\partial x}\right)+\frac{\partial}{\partial y}\left(k_{eff}\frac{\partial T}{\partial y}\right)+S_T \tag{32}$$

$$\frac{\partial(\rho UY_i)}{\partial x}+\frac{\partial(\rho VY_i)}{\partial y}=\frac{\partial}{\partial x}\left(\rho D_{i,m}^{eff}\frac{\partial Y_i}{\partial x}\right)+\frac{\partial}{\partial y}\left(\rho D_{i,m}^{eff}\frac{\partial Y_i}{\partial y}\right)+S_{sp} \tag{33}$$

The density of the gas mixture (ρ) can be written as [25].

$$\rho=\frac{1}{\sum_{i=1}^{N}Y_i/\rho_i} \tag{34}$$

where ρ_i and Y_i are the density and mass fraction of gas species *i*. ρ_i can be determined from the ideal gas law (Eq. 35).

$$\rho_i=\rho_{i,298K}\frac{298}{T} \tag{35}$$

The viscosity of the gas mixture (μ) can be calculated as [38]

$$\mu=\sum_{i=1}^{n}\frac{y_i\mu_i}{\sum_{j=1}^{n}\left(y_j\sqrt{\frac{M_j}{M_i}}\right)} \tag{36}$$

where M_i is molecular weight of species *i* (kg.kmol^{-1}).

The effective heat conductivity (k_{eff}) and heat capacity ($c_{p,eff}$) of the gas mixture depends on the gas composition. In the porous electrodes, k_{eff} and $c_{p,eff}$ can be calculated as a function of the electrode porosity (ε) [39,40]

$$k_{eff} = \varepsilon k_f + (1-\varepsilon) k_s \tag{37}$$

$$c_{p,eff} = \varepsilon c_{p,f} + (1-\varepsilon) c_{p,s} \tag{38}$$

where k_f and k_s are the heat conductivity of the gas mixture and the solid structure, respectively. $c_{p,f}$ and $c_{p,s}$ are the heat capacity of the gas mixture and the solid structure, respectively.

The effective diffusion coefficients $D_{i,m}^{eff}$ in species' equation (Eq. 33) can be calculated as [30],

$$\frac{1}{D_{i,m}^{eff}} = \begin{cases} \dfrac{\xi}{\varepsilon}\left(\dfrac{\sum \dfrac{X_j}{D_{ij}}}{1-X_i} + \dfrac{3}{2r_p}\sqrt{\dfrac{\pi M_i}{8RT}} \right), & \text{in porous electrodes} \\ \dfrac{\sum \dfrac{X_j}{D_{ij}}}{1-X_i}, & \text{in gas channels} \end{cases} \tag{39}$$

$$D_{ij} = \frac{0.0026 T^{1.5}}{p\sqrt{\dfrac{2M_i M_j}{M_j + M_i}}\left(\dfrac{\sigma_i + \sigma_j}{2}\right)^2 \Omega_D} \tag{40}$$

$$\Omega_D = \frac{1.06036}{\left(\dfrac{k_b T}{\varepsilon_{i,j}}\right)^{0.1561}} + \frac{0.193}{\exp\left(0.47635\left(\dfrac{k_b T}{\varepsilon_{i,j}}\right)\right)} + \frac{1.03587}{\exp\left(1.52996\left(\dfrac{k_b T}{\varepsilon_{i,j}}\right)\right)} + \frac{1.76474}{3.89411\left(\dfrac{k_b T}{\varepsilon_{i,j}}\right)} \tag{41}$$

where ξ/ε is the ratio of tortuosity to porosity. r_p is the average pore radius. D_{ij} is the binary diffusion coefficient of i and j. σ is the mean characteristic length and Ω_D is a dimensionless diffusion collision term. k_b is the Boltzmann's constant (1.38066×10^{-23} J.K^{-1}). The values of

σ_i and $\varepsilon_{i,j}$ are summarized in Table 1 [38]. X_i is the molar fraction of specie i and can be related to the mass fraction (Y_i) as.

$$Y_i = X_i \left(\frac{M_i}{\sum_{i=1}^{N} X_i M_i} \right) \tag{42}$$

The source terms in the momentum equations in x and y directions (Eqs. 30 and 31) are,

$$\begin{cases} S_x = -\dfrac{\mu U}{B_g} \\ S_y = -\dfrac{\mu V}{B_g} \end{cases} \tag{43}$$

where B_g is the permeability (m^2). Typical value of permeability (i.e. $2\times10^{-10}\,m^2$) is used for the SOFC electrodes while infinitely large value (i.e. $10^{20}\,m^2$) is used for the gas channels [25], so that the momentum equations can be applied to both the gas channels and the porous electrodes.

The source term (S_T, $W.m^{-3}$) in the energy equation (Eq. 32) accounts for heat associated with DIR reaction and WGSR, heat from electrochemical reactions, and heat from irreversible overpotential losses. In the present simulation, the source term in the porous anode comes from the reaction heat for DIR reaction and WGSR. The heat from electrochemical reaction and irreversible overpotential losses are evenly applied to the dense electrolyte. Thus, the source term S_T can be written as [30,41],

$$S_T = \begin{cases} R_{MSR}H_{MSR} + R_{MCDR}H_{MCDR} + R_{WGSR}H_{WGSR}, & \text{in porous anode} \\ -\dfrac{J_{H_2}T\Delta S_{H_2} + J_{CO}T\Delta S_{CO}}{2FL} + \dfrac{J_{H_2}\eta_{t,H_2}}{L} + \dfrac{J_{CO}\eta_{t,CO}}{L}, & \text{in electrolyte} \end{cases} \tag{44}$$

where ΔS_{H_2} and ΔS_{CO} are the entropy changes for electrochemical reactions associated with H_2 fuel and CO fuel, respectively. η_{t,H_2} and $\eta_{t,CO}$ are the total overpotential losses for H_2 fuel and CO fuel. Here the concentration overpotential is not included since it is included in the Nernst potential. Including concentration overpotential into the source term can increase the heat

generation rate. However, since concentration overpotential is usually very small (unless very high current density), its effect on the source term is negligibly small.

The source term (S_{sp} , kg.m^{-3}.s^{-1}) in the species equation (Eq. 33) represents species consumption or generation due to the chemical and electrochemical reactions. Taking H_2 and CO as examples, the source term (S_{H_2}) in the species equation can be written as [30,41],

$$S_{H_2} = \begin{cases} 3R_{MSR}M_{H_2} + 2R_{MCDR}M_{H_2} + R_{WGSR}M_{H_2}, & \text{in porous anode} \\ -\dfrac{J_{H_2}M_{H_2}}{2F\Delta y}, & \text{at the anode-electrolyte interface} \end{cases} \tag{45}$$

$$S_{CO} = \begin{cases} R_{MSR}M_{CO} + 2R_{MCDR}M_{CO} - R_{WGSR}M_{CO}, & \text{in porous anode} \\ -\dfrac{J_{CO}M_{CO}}{2F\Delta y}, & \text{at the anode-electrolyte interface} \end{cases} \tag{46}$$

where Δy is the control volume width in y-direction (Fig. 1) at the anode-electrolyte interface. At the cathode-electrolyte interface, the source term (S_{O_2}) can be written as,

$$S_{O_2} = \begin{cases} 0, & \text{in porous cathode} \\ -\dfrac{\left(J_{CO} + J_{H_2}\right)M_{O_2}}{4F\Delta y}, & \text{at the cathode-electrolyte interface} \end{cases} \tag{47}$$

3. Numerical Methodologies

The boundary conditions of the 2D model have been reported in the previous publications [25,43]. The governing equations are discretized and solved with the finite volume method (FVM). The pressure and velocity are coupled with the SIMPLEC algorithm [42]. The iteration scheme is shown in Figure 2. The program starts from initialization. Initial pressure, temperature, velocity, gas composition etc, are assigned to the whole computational domain. Based on the initial data, the chemical model is solved to determine the local chemical reaction rates and reaction heat. Then the electrochemical model is solved to determine the local electrochemical reaction rate (current density) as well as corresponding heat. Subsequently,

source terms in the CFD model are calculated. After the CFD model is solved, the flow field, temperature field and gas composition can be updated, which are used to solve the chemical model and electrochemical model again. Computation is repeated until convergence is achieved. The equations are solved with an in-house code in FORTRAN. The CFD code has been validated by comparing the CFD simulation results with data from the literature [43]. The friction factor and Nusselt number of rectangular duct have been computed and compared with data by Prof. Yuan [39]. Excellent agreement between the CFD simulation results with Prof. Yuan's data [39] was found and reported in the previous publication [43]. To avoid duplication, the comparison is not repeated here.

4. Results and Analysis

In this section, simulations are performed to investigate the effects of various operating parameters on performance of SOFCs with MCDR. The values of input parameters are summarized in Table 2. More detailed information about the parameters can be found from the previous publications [25,29]. As SOFCs are typically operated at a potential of 0.5 – 0.8V, simulations are performed for operating potential of 0.5V and 0.8V. For SOFC with steam reforming of CH_4, usually 30% pre-reformed CH_4 fuel is used. The experimental study in the literature has demonstrated that it's feasible to supply CH_4/CO_2 mixture directly to SOFC and the SOFC achieves good performance at the molar ratio of 1:1 [44-46]. In the present study, the molar ratio of CH_4/CO_2 is set to be 1:1 at the SOFC inlet. The values used in parametric simulations are summarized in Table 3.

4.1. Base case

Simulation is performed at an inlet temperature of 1073K, operating potential of 0.5V, and $J^0_{CO,a} = 0.3J^0_{H_2,a}$ (for simplicity, $J^0_{CO} = 0.3J^0_{H_2}$ is used). The computed current density

distribution is shown in Figure 3. It is found that the current density increases at the inlet and then decreases along the flow channel. The increase in current density near the inlet is mainly caused by reforming of CH_4 that generates H_2 and CO. The reduction in current density in the downstream is mainly caused by lower temperature, which is discussed later. In addition, the current density generated from H_2 fuel is higher than that from CO fuel, as the electrochemical oxidation of H_2 is faster. The total current density is found to be comparable to that of SOFC fed with CH_4/H_2O mixture [17,25], indicating that SOFC with MCDR is feasible.

The reaction rate of MCDR is found to be the highest at the inlet and decrease along the gas channel significantly (Fig. 4a), due to reduced temperature (Fig. 4d) and lower CH_4 molar fraction in the downstream (Fig. 5a). The computed MCDR rate at the inlet (at 1073K) is about 224mol.m^{-3}.s^{-1}, which is consistent with the measured data from [32]. In addition, Moon and Ryu [24] measured the electrocatalytic reforming of CH_4 by CO_2 on NiO-MgO catalyst at 1073K. The measured reaction rate for CH_4 is about 0.47 μmol.cm^{-2}.s^{-1}. As the thickness of the catalyst layer is about 20 μm, the measured reaction rate is converted to be about 235mol.m^{-3}.s^{-1}, which is also consistent with the computed data in the present study. Prof. Yentekakis's group has worked on testing of SOFC performance with MCDR for several years [44-46]. In their study, the MCDR reaction rate on Ni-YSZ cermet electrode was measured [44]. At a temperature of 1073K, the peak MCDR reaction rate of about 1.5 μmol.s^{-1} was achieved [44]. Considering that the electrode surface area is about 1.8 cm^2 and the thickness of the electrode is about 20 μm, the measured MCDR reaction rate is about 416 mol.m^{-3}.s^{-1}. The measured reaction rate is higher than but on the same order with the computed data in the present study. The difference may be caused by the good activity of the Ni-YSZ cermet anode (prepared by wet impregnation) toward MCDR reaction [44]. The MCDR reaction rate is highly dependent on the material and morphology of the catalyst layer. As can be seen from another study by Prof. Yentekakis [45], the peak MCDR reaction rate is increased to be about 2 μmol.s^{-1} at

1073K when Ni(Au)-GDC (gadolinia doped ceria) cermet electrode is used. The WGSR is found to be negative in the porous SOFC anodes (Fig. 4b), as the low concentration of CO and H_2O favors backward reaction. For comparison, the reaction rate of MSR is found to be much lower than that of MCDR and WGSR (Fig. 4c), which is quite different from conventional SOFC with MSR [25]. The peak MSR is found at the anode-electrolyte interface near the inlet, due to high CH_4 concentration (Fig. 5a) and high temperature (Fig. 4d) near the SOFC inlet and relatively high concentration of H_2O at the anode-electrolyte interface (Fig. 5c). The temperature field in the SOFC depends on: (1) heat generation from electrochemical reactions associated with H_2 fuel and CO fuel; (2) heat generation from irreversible overpotential loss; (3) heat consumption by endothermic MCDR, which is high due to high MCDR reaction rate; (4) heat consumption by endothermic MSR; and (5) heat generation by exothermic WSGR. The large temperature drop in the SOFC along the gas channel means that the heat consumption by (3), (4), and (5) (negative WGSR) exceeds the heat generation from (1) and (2). The reduction in temperature along the flow channel considerably decreases the reaction rate of MCDR (Fig. 4a), leading to lower fuel conversion in the downstream. Due to the high MCDR rate, the molar fractions of both CH_4 and CO_2 decrease considerably in the SOFC (Fig. 5a and 5b). For comparison, the molar fraction of H_2O increases considerably in the SOFC (Fig. 5c), due to negative WGSR and electrochemical oxidation of H_2 fuel. The considerable difference in H_2O molar fraction between the anode-electrolyte interface and the anode surface indicates high resistance of the porous anode to gas transport.

From this section, it can be seen that the performance of SOFC with MCDR is comparable to that of SOFC with MSR. In addition, MCDR considerably influences the SOFC performance by affecting the temperature field and gas composition in the cell. To reduce the negative temperature gradient in the SOFC, additional heat supply is needed. It can be achieved by utilizing the waste heat from the exhaust gas stream, or by heat supply from the furnace.

Alternatively, pre-reforming of the CH_4 fuel can be adopted using an external reformer [47], thus it's possible to adjust the temperature gradient in the SOFC by controlling the extent of pre-reforming. However, it is out of the objective of the present study and detailed discussions are not provided in this paper.

4.2. Effect of operating temperature

Simulations are performed at an inlet temperature of 973K and 1173K to investigate the temperature effect on SOFC performance. The computed current density is shown in Figure 6. It can be seen that the current density is increased significantly when the inlet temperature is increased from 973K to 1173K.

With an increase in temperature, the reaction rates of MCDR, MSR, and negative WGSR are all increased (Fig. 7). For example, the peak reaction rates for MCDR, MSR, and WGSR are increased from about 151mol.m^{-3}.s^{-1}, 0.0935mol.m^{-3}.s^{-1}, and -3.92mol.m^{-3}.s^{-1} at 973K to about 303mol.m^{-3}.s^{-1}, 21.8mol.m^{-3}.s^{-1}, and -76.8mol.m^{-3}.s^{-1} at 1173K. The high reaction rates at a high temperature tend to increase the concentrations of H_2 fuel and CO fuel, which in turn increases the Nernst potentials. In addition, the overpotential losses decrease with increasing temperature [29]. The combined effects of temperature on the Nernst potential and the overpotential losses cause the current densities by both the H_2 fuel and CO fuel to increase with increasing temperature. The increased chemical reaction rates (MCDR, negative WGSR, and MSR) consume more heat and tend to further reduce the SOFC temperature. On the other hand, the higher current density at a higher temperature tends to generate more heat by electrochemical reactions and the overpotential losses. As a result, the temperature reduction for 1173K case (60K: 1113K at the outlet) is only slightly larger than the 973K (56K: 917K at the outlet) (Figs. 7g and 7h). Since the reaction rates for all chemical reactions are higher, more CH_4 and CO_2 are

converted to CO and H_2, leading to larger drops in molar fractions of CH_4 and CO_2 in the cell at 1173K (Figs. 8).

4.3. Effect of electrochemical reaction rate of CO

In the literature, only very limited experimental and theoretical data on CO electrochemical reaction rates are available [26,28]. Thus, it is necessary to examine the effect of CO electrochemical oxidation rate on SOFC performance. In this section, simulation is performed at $J^0_{CO} = 0.6J^0_{H_2}$ and the results are compared with the $J^0_{CO} = 0.3J^0_{H_2}$ case. The total current density and current density by the H_2 and CO fuels are shown in Fig. 9. An increase in CO electrochemical oxidation rate significantly increases the current density by CO fuel (Fig. 9c), which in turn increases the total current density (Fig. 9a). Interestingly, the current density by H_2 fuel is also slightly increased as $J^0_{CO} = 0.3J^0_{H_2}$ is changed to $J^0_{CO} = 0.6J^0_{H_2}$ (Fig. 9b). The computed reaction rates of MCDR and MSR at $J^0_{CO} = 0.6J^0_{H_2}$ are very close to those at $J^0_{CO} = 0.3J^0_{H_2}$ (Fig. 10a and 10c). However, the WGSR reaction rates are found to be higher at $J^0_{CO} = 0.6J^0_{H_2}$ than at $J^0_{CO} = 0.3J^0_{H_2}$ (Fig. 10b). This is because the high electrochemical oxidation of CO tends to consume more CO, which favors the negative WGSR. The temperature at the SOFC outlet is about 1019K at $J^0_{CO} = 0.6J^0_{H_2}$ (Fig. 10d), slightly higher than at $J^0_{CO} = 0.3J^0_{H_2}$ (1017K). This small difference is caused by the higher current density at $J^0_{CO} = 0.6J^0_{H_2}$, which produces more heat in SOFC. As the rate of MCDR is almost independent of the CO electrochemical oxidation rate, the molar fraction of CH_4 is found to be almost unchanged for these two cases (Fig. 11a). For the molar fraction of CO_2, it is related to the WGSR reaction and the electrochemical oxidation of CO. The more negative WGSR reaction rate at $J^0_{CO} = 0.6J^0_{H_2}$ tends to consume more CO_2. On the other hand, the high current density by

CO fuel tends to generate more CO_2 at $J_{CO}^0 = 0.6J_{H_2}^0$. As a result, the molar fraction of CO_2 at $J_{CO}^0 = 0.6J_{H_2}^0$ shows negligibly small difference from that at $J_{CO}^0 = 0.3J_{H_2}^0$ (Fig. 11b). For comparison, the H_2O molar fraction in the SOFC is obviously higher at $J_{CO}^0 = 0.6J_{H_2}^0$ than at $J_{CO}^0 = 0.3J_{H_2}^0$, as the slightly higher current density by H_2 fuel produces more H_2O in the cell (Fig. 11c).

4.4. Effect of operating potential

The operating potential is an important parameter for SOFC operation. In this section, simulation is performed at an operating potential of 0.8V and the results are compared with that at 0.5V. The current densities are shown in Fig. 12. As expected, the current density is decreased considerably as the potential is increased from 0.5V to 0.8V. The reaction rates of MCDR, WGSR and MSR, as well as the temperature are shown in Figs. (13a-d). Although the difference in MCDR reaction rates between the two cases (0.5V and 0.8V) is negligibly small (Fig. 13a), the WGSR reaction rate at 0.8V is considerably different from that at 0.5V (Fig. 13b). As can be seen, the peak WGSR reaction rate is lower at 0.8V than at 0.5V. Moreover, the WGSR reaction rate is more uniform along the anode depth at 0.8V (Fig. 13b). For comparison, high WGSR reaction rate mainly occurs near the anode surface at 0.5V (Fig. 4b). Since the current density is lower at a higher operating potential, less heat is generated and more heat reduction is observed in the cell at 0.8V (Fig. 13d). The lower temperature in the downstream of the cell at 0.8V in turn results in slightly lower reaction rate of MCDR (cannot be clearly seen from Fig. 13a) than that at 0.5V. Consequently, the gas composition variations in the SOFC are found smaller at 0.8V than at 0.5V (Figs. 14a-c).

5. Conclusions

A 2D numerical model is developed to characterize the performance of SOFCs fed with CO_2 and CH_4 mixtures. The model fully considers the mass transport and heat transfer, the chemical reaction kinetics, and electrochemical reaction kinetics.

Simulations are performed at various inlet temperatures, CO electrochemical oxidation rates, and operating potentials. The computed CO_2 reforming reaction rate is consistent with the literature data. The MCDR reaction rate is the highest near the inlet while the MSR reaction rate is negligibly small. The WGSR is found to be negative due to low concentrations of CO and H_2 in the cell. The MCDR, MSR and negative WGSR consumes heat, leading to a decrease in temperature along the SOFC channel. Increasing the inlet temperature from 973K to 1173K considerably increases the current density of SOFC, as the high chemical reaction rates produces more CO and H_2 fuels, which in turn increases the Nernst potentials. Increasing the CO electrochemical oxidation rate not only significantly increases the current density by CO fuel, but also increases moderately the current density by H_2 fuel, leading to improved SOFC performance. The current densities decrease considerably with increasing operating potential, which in turn generates less heat and leads to lower temperature in the downstream of SOFC.

The parametric simulations reveal that the SOFC fed with CO_2 and CH_4 is feasible. The SOFC electric power output can be enhanced by developing catalysts with high activity towards CO electrochemical oxidation, operating the cell at a high temperature, or a low potential. The model can serve as a useful tool for optimization of the SOFC systems.

Acknowledgements:

This research was supported by a grant (Project Number: PolyU 5238/11E) from Research Grant Council (RGC) of Hong Kong.

References:

[1] Singhal SC, Kendall K, High temperature solid oxide fuel cells – Fundamentals, design and applications, Elsevier, New York (2003).
[2] Colpan CO, Dincer I, Hamdullahpur F, Thermodynamic modeling of direct internal reforming solid oxide fuel cells operating with syngas. International Journal of Hydrogen Energy 2007; **32**:787–795.
[3] Su C, Ran R, Wang W, Shao ZP, Coke formation and performance of an intermediate-temperature solid oxide fuel cell operating on dimethyl ether fuel, Journal of Power Sources 2011; 196:1967-1974.
[4] Liu MF, Peng RR, Dong DH, Gao JF, Liu XQ, Meng GY, Direct liquid methanol-fueled solid oxide fuel cell, Journal of Power Sources 2008; 185:188-192.
[5] Ma QL, Peng RR, Lin YJ, Gao JF, Meng GY, A high-performance ammonia-fueled solid oxide fuel cell, Journal of Power Sources 2006; 161: 95-98.
[6] Ni M, Leung DYC, Leung MKH, Modeling of methane fed solid oxide fuel cells: comparison between proton conducting electrolyte and oxygen ion conducting electrolyte, Journal of Power Sources 2008; 183: 133-142.
[7] Ni M, Leung DYC, Leung MKH, Mathematical modeling of ammonia-fed solid oxide fuel cells with different electrolytes, International Journal of Hydrogen Energy 2008; 33:5765-5772.
[8] Zhao TS, Micro fuel cells – Principles and Applications, Elsevier, New York (2009).
[9] Timmermann H, Sawady W, Reimert R, Ivers-Tiffee E, Kinetics of (reversible) internal reforming of methane in solid oxide fuel cells under stationary and APU conditions, Journal of Power Sources 2010; 195: 214-222.
[10] Park J, Li PW, Bae J, Analysis of chemical, electrochemical reactions and thermo-fluid flow in methane-feed internal reforming SOFCs: Part I- modeling and effect of gas concentrations, International Journal of Hydrogen Energy 2012; 37: 8512-8531.
[11] Haberman BA, Young JB, Three-dimensional simulation of chemically reacting gas flows in the porous support structure of an integrated-planar solid oxide fuel cell, International Journal of Heat and Mass Transfer 2004; 47: 3617–3629.
[12] Vakouftsi E, Mamellos G, Athanasiou C, Coutelieris FA, A detailed model for transport processes in a methane fed planar SOFC, Chemical Engineering Research and Design 2011; 89: 224-229.
[13] Ferguson JR, Fiard JM, Herbin R, Three-dimensional numerical simulation for various geometries of solid oxide fuel cells, Journal of Power Sources 1996; 58: 109-122.
[14] Ho TX, Kosinski P, Hoffmann AC, Vik A, Transport, chemical and electrochemical processes in a planar solid oxide fuel cell: detailed three-dimensional modeling, Journal of Power Sources 2010; 195: 6764-6773.
[15] Recknagle KP, Ryan EM, Koeppel BJ, Mahoney LA, Khaleel MA, Modeling of electrochemistry and steam-methane reforming performance for simulating pressurized solid oxide fuel cell stacks, Journal of Power Sources 2010; 195: 6637-6644.
[16] Ni M, Leung DYC, Leung MKH, Electrochemical modeling and parametric study of methane fed solid oxide fuel cells, Energy Conversion and Management 2009; 50: 268-278.
[17] Ni M, Electrolytic effect in solid oxide fuel cells running on steam/methane mixture, Journal of Power Sources 2011; 196: 2027-2036.
[18] Bessler WG, Gewies S, Vogler M, A new framework for physically based modeling of solid oxide fuel cells, Electrochimica Acta 2007; 53: 1782-1800.
[19] Janardhanan VM, Heuveline V, Deutschmann O, Performance analysis of a SOFC under direct internal reforming conditions, Journal of Power Sources 2007; 172: 296-307.

[20] Hecht ES, Gupta GK, Zhu HY, Dean AM, Kee RJ, Maier L, Deutschmann O, Methane reforming kinetics within a Ni-YSZ SOFC anode support, Applied Catalysis A: General 2005; 295: 40-51.
[21] Janardhanan VM, Deutschmann O, CFD analysis of a solid oxide fuel cell with internal reforming: coupled interactions of transport, heterogeneous catalysis and electrochemical processes, Journal of Power Sources 2006; 162: 1192-1202.
[22] Zhu HY, Kee RJ, Two-dimensional model of distributed charge transfer and internal reforming within unit cells of segmented-in-series solid oxide fuel cells, Journal of Power Sources 2011; 196: 7654-7664.
[23] Zhu HY, Kee RJ, Janardhanan VM, Deutschmann O, Goodwin DG, Modeling elementary heterogeneous chemistry and electrochemistry in solid oxide fuel cells, Journal of the Electrochemical Society 2005; 152: A2427-A2440.
[24] Moon DJ, Ryu JW, Electrocatalytic reforming of carbon dioxide by methane in SOFC system, Catalysis Today 2003; 87: 255-264.
[25] Ni M, Modeling of SOFC running on partially pre-reformed gas mixture, International Journal of Hydrogen Energy 2012; 37: 1731-1745.
[26] Matsuzaki Y, Yasuda I, Electrochemical oxidation of H_2 and CO in a H_2-H_2O-CO-CO_2 system at the interface of a Ni-YSZ cermet electrode and YSZ electrolyte, Journal of the Electrochemical Society 2000; 147: 1630-1635.
[27] Janardhanan VM, Deutschmann O, Numerical study of mass and heat transport in solid-oxide fuel cells running on humidified methane, Chemical Engineering Science 2007; 62: 5473–5486.
[28] Andersson M, Yuan JL, Sunden B, Grading the amount of electrochemical active sites along the main flow direction of an SOFC, Journal of the Electrochemical Society 2013; 160: F1-F12.
[29] Ni M, Leung MKH, Leung DYC, Parametric study of solid oxide fuel cell performance, Energy Conversion and Management 2007; 48: 1525-1535.
[30] Ni M, 2D thermal modeling of a solid oxide electrolyzer cell (SOEC) for syngas production by H_2O/CO_2 co-electrolysis, International Journal of Hydrogen Energy 2012; 37: 6389-6399.
[31] Chan SH, Khor KA, Xia ZT, A complete polarization model of a solid oxide fuel cell and its sensitivity to the change of cell component thickness, Journal of Power Sources 2001; 93: 130-140.
[32] Gokon N, Osawa Y, Nakazawa D, Kodama T, Kinetics of CO_2 reforming of methane by catalytically activated metallic foam absorber for solar receiver-reactors, International Journal of Hydrogen Energy 2009; 34: 1787-1800.
[33] Soloviev SO, Kapran AY, Orlyk SN, Gubareni EV, Carbon dioxide reforming of methane on monolithic Ni/Al_2O_3-based catalysts, Journal of Natural Gas Chemistry 2011; 20: 184-190.
[34] Chase MW, NIST-JANAF thermochemical tables, (4th ed.), American Chemical Society, American Institute of Physics for the National Institute of Standards and Technology (1998).
[35] Zheng KQ, Sun Q, Ni M, On the local thermal non-equilibrium in SOFCs considering internal reforming and ammonia thermal cracking reaction, Energy Technology 2012, in press. DOI: 10.1002/ente.201200014.
[36] Andersson M, Yuan JL, Sunden B, SOFC modeling considering electrochemical reactions at the active three phase boundaries, International Journal of Heat and Mass Transfer 2012; 55: 773-788.
[37] Wang CY, Fundamental models for fuel cell engineering, Chemical Reviews 2004; 104: 4727-4765.
[38] Reid RC, Prausnitz JM, Poling BE, The properties of gases & liquids (4th edition). McGraw-Hill Book Company, New York (1987).

[39] Yuan JL, Rokni M, Sunden B, Three-dimensional computational analysis of gas and heat transport phenomena in ducts relevant for anode-supported solid oxide fuel cells, International Journal of Heat and Mass Transfer 2003; 46: 809-821.
[40] Yuan JL, Lv XR, Sunden B, Yue DT, Analysis of parameter effects on transport phenomena in conjunction with chemical reactions in ducts relevant for methane reformers, International Journal of Hydrogen Energy 2007; 32: 3887-3898.
[41] Ni M, On the source terms of species equations in fuel cell modeling, International Journal of Hydrogen Energy 2009; 34: 9543-9544.
[42] Patankar SV, Numerical heat transfer and fluid flow, McGraw-Hill, New York (1980).
[43] Ni M, 2D thermal-fluid modeling and parametric analysis of a planar solid oxide fuel cell, Energy Conversion and Management 2010; 51: 714-721.
[44] Goula G, Kiousis V, Nalbandian L, Yentekakis IV, Catalytic and electrocatalytic behavior of Ni-based cermet anodes under internal dry reforming of CH4+CO2 mixtures in SOFCs, Solid State Ionics 2006; 177: 2119-2123.
[45] Yentekakis IV, Open – and closed-circuit study of an intermediate temperature SOFC directly fueled with simulated biogas mixtures, Journal of Power Sources 2006; 160: 422-425.
[46] Papadam T, Goula G, Yentekakis IV, Long-term operation stability tests of intermediate and high temperature Ni-based anodes' SOFCs directly fueled with simulated biogas mixtures, International Journal of Hydrogen Energy 2012; 37: 16680-16685.
[47] Ni M, 2D heat and mass transfer modeling of methane steam reforming for hydrogen production in a compact reformer, Energy Conversion and Management 2013; 65: 155-163.

List of Tables

List of Figures

Table 1. Values of σ_i and ε_i / k for calculating the diffusion coefficients [38]

	CO	CO_2	H_2	O_2	CH_4	N_2	H_2O
σ_i	3.69	3.941	2.827	3.467	3.758	3.798	2.641
ε_i / k	91.7	195.2	59.7	106.7	148.6	71.4	809.1

Table 2. Parameters used in simulation

Parameter	Value
Operating temperature, T (K)	1073
Operating pressure, P (bar)	1.0
Electrode porosity, ε	0.4
Electrode tortuosity, ξ	3.0
Average pore radius, r_p (μm)	0.5
Anode-supported electrolyte:	
Anode thickness d_a (μm)	500
Electrolyte thickness, L (μm)	100
Cathode thickness, d_c (μm)	100
Height of gas flow channel (mm)	1.0
Length of the planar SOFC (mm)	20
Thickness of interconnector (mm)	0.5
Inlet velocity at anode: U_0 ($m.s^{-1}$)	1.0
Cathode inlet gas molar ratio: O_2/N_2	0.21/0.79
Anode inlet gas molar ratio: CH_4/ CO_2	0.5/0.5
SOFC operating potential (V)	0.5
Thermal conductivity of SOFC component ($W.m^{-1}.K^{-1}$)	
Anode	11.0
Electrolyte	2.7
Cathode	6.0
Interconnect	1.1

Table 3. List of parametric simulations

Base case	T = 1073K; Potential = 0.5V
Effect of inlet temperature	T = 973K and 1173K
Effect of different exchange current density for CO fuel	T = 1073K; $J_{CO}^{0} = 0.6J_{H_2}^{0}$ vs $J_{CO}^{0} = 0.3J_{H_2}^{0}$
Effect of operating potential	T = 1073K; Potential = 0.8V vs Potential = 0.5V

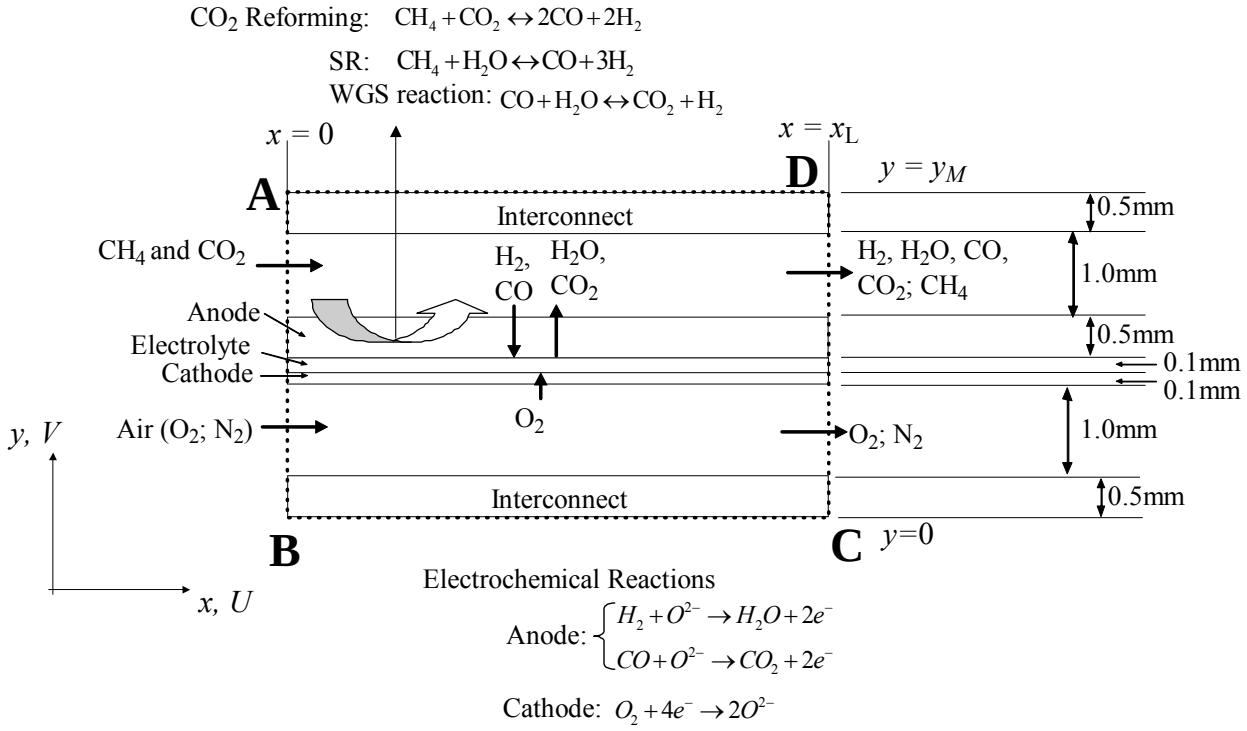
CO2 Reforming: CH4 + CO2 ↔ 2CO + 2H2
SR: CH4 + H2O ↔ CO + 3H2
WGS reaction: CO + H2O ↔ CO2 + H2
x = 0
x = xL
A
D
y = yM
Interconnect
0.5mm
CH4 and CO2
H2, CO
H2O, CO2
H2, H2O, CO, CO2; CH4
1.0mm
Anode
Electrolyte
Cathode
0.5mm
0.1mm
0.1mm
O2
y, V
Air (O2; N2)
O2; N2
1.0mm
Interconnect
0.5mm
B
C
y=0
x, U
Electrochemical Reactions
Anode: H2 + O2− → H2O + 2e−
CO + O2− → CO2 + 2e−
Cathode: O2 + 4e− → 2O2−

Figure 1

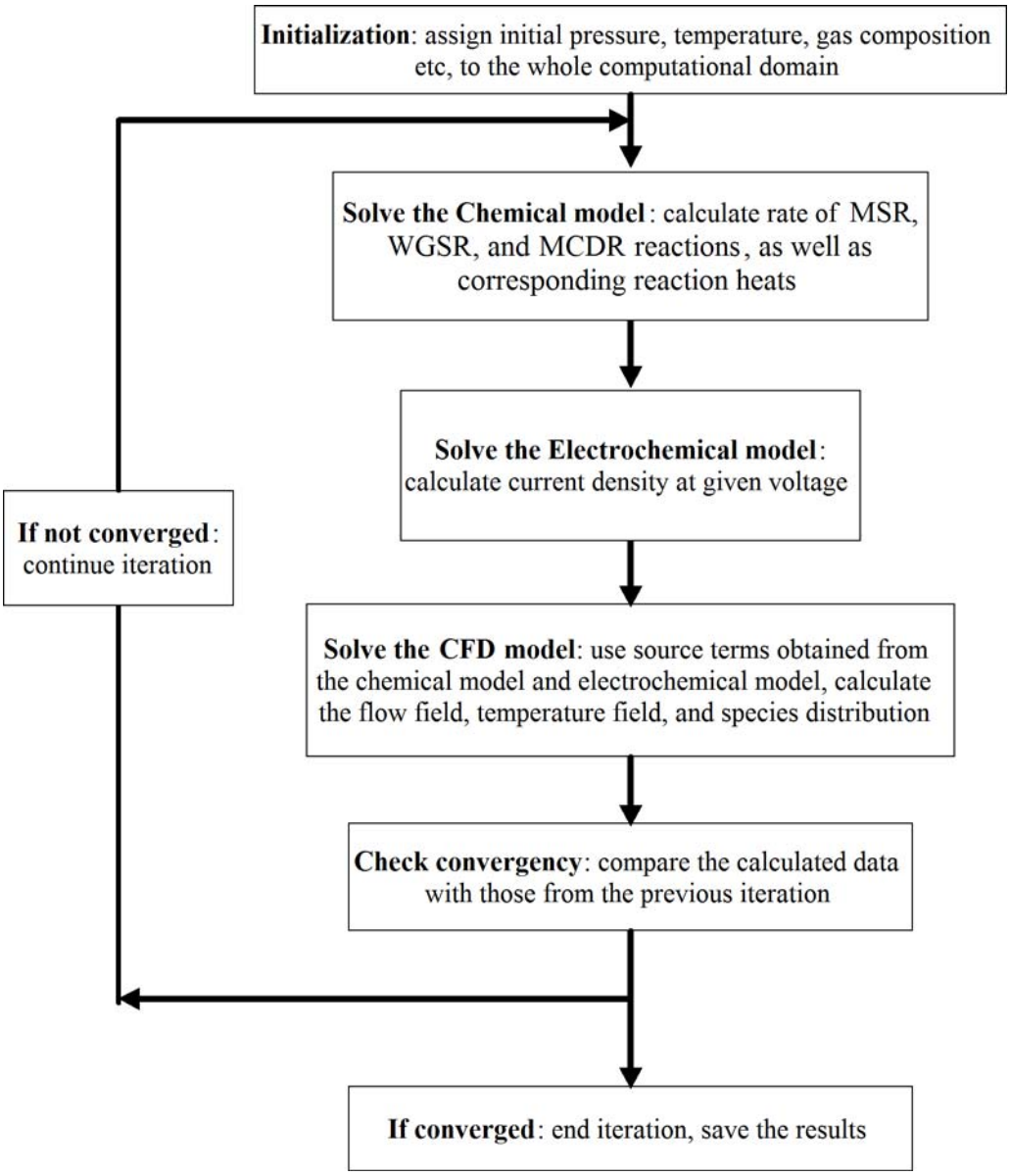
Initialization: assign initial pressure, temperature, gas composition etc, to the whole computational domain
Solve the Chemical model: calculate rate of MSR, WGSR, and MCDR reactions, as well as corresponding reaction heats
Solve the Electrochemical model: calculate current density at given voltage
Solve the CFD model: use source terms obtained from the chemical model and electrochemical model, calculate the flow field, temperature field, and species distribution
Check convergency: compare the calculated data with those from the previous iteration
If converged: end iteration, save the results
If not converged: continue iteration

Figure 2

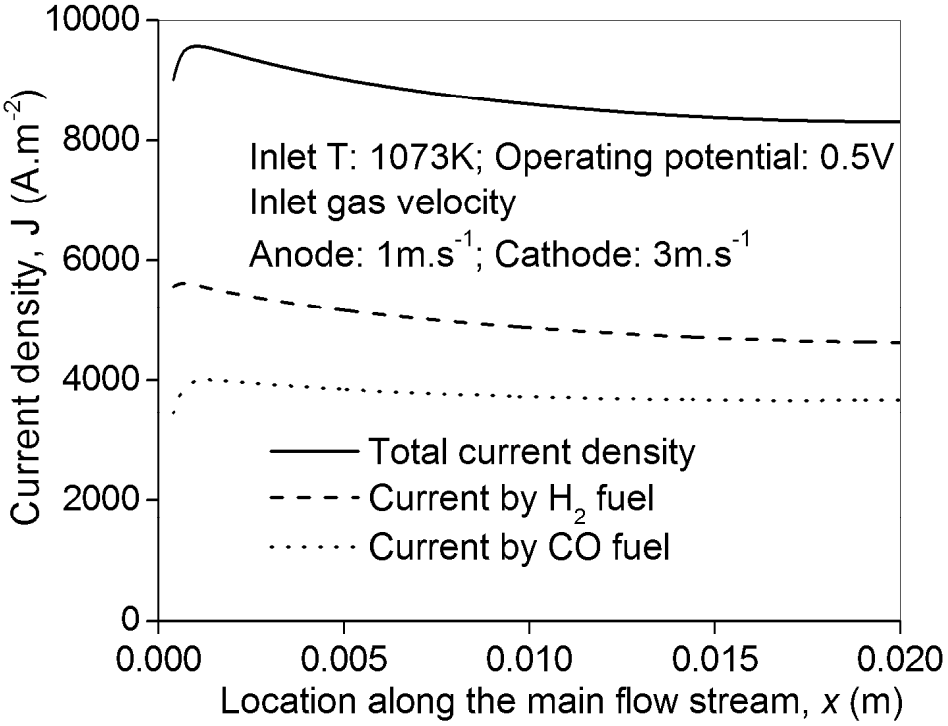
10000
8000
6000
4000
2000
0
Current density, J (A.m-2)
Inlet T: 1073K; Operating potential: 0.5V
Inlet gas velocity
Anode: 1m.s-1; Cathode: 3m.s-1
Total current density
Current by H2 fuel
Current by CO fuel
0.000
0.005
0.010
0.015
0.020
Location along the main flow stream, x (m)

Figure 3

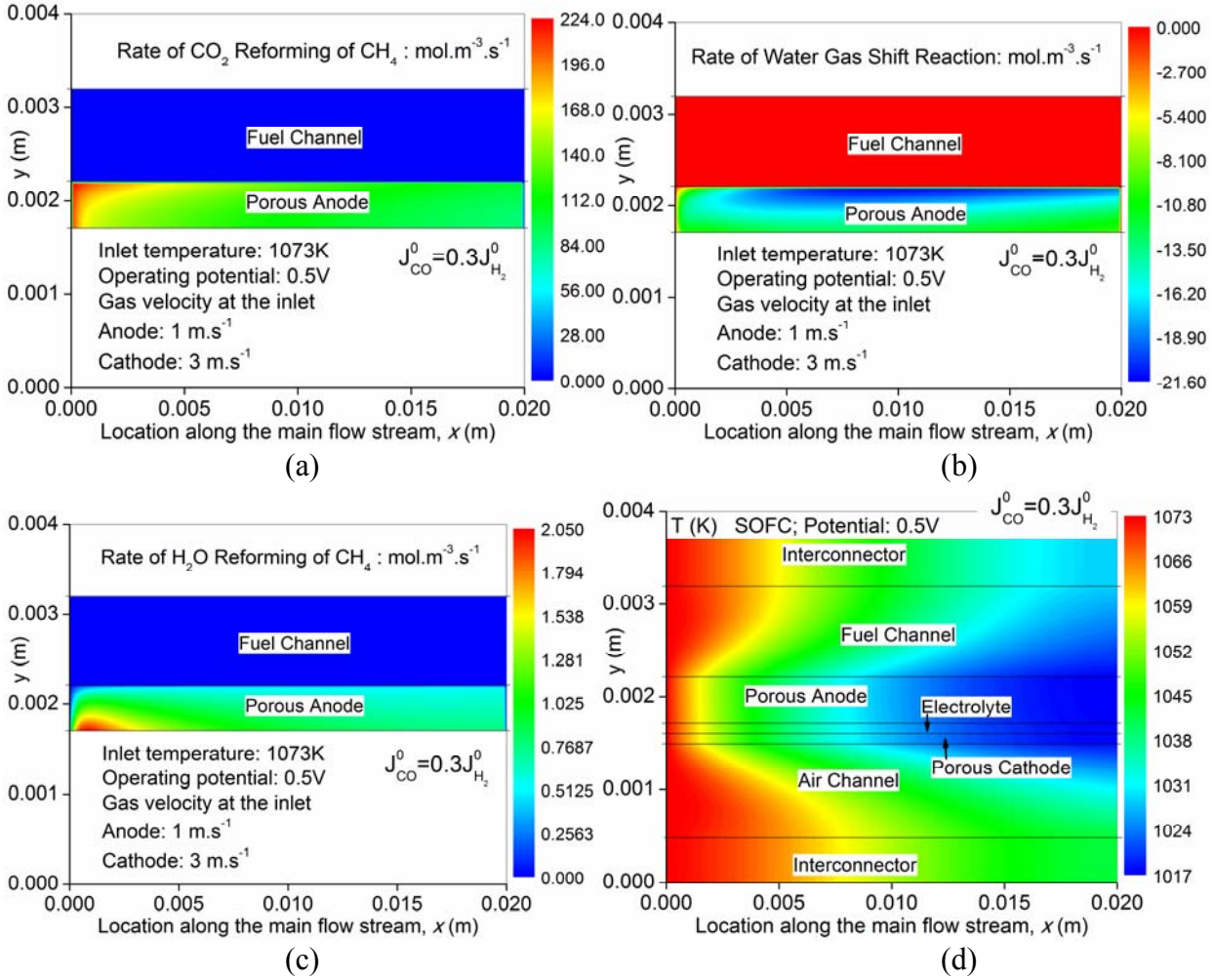
Rate of CO_2 Reforming of CH_4 : mol.m^{-3}.s^{-1}
Fuel Channel
Porous Anode
Inlet temperature: 1073K
Operating potential: 0.5V
Gas velocity at the inlet
Anode: 1 m.s^{-1}
Cathode: 3 m.s^{-1}
$J^0_{CO}=0.3J^0_{H_2}$
y (m)
Location along the main flow stream, x (m)
(a)
Rate of Water Gas Shift Reaction: mol.m^{-3}.s^{-1}
(b)
Rate of H_2O Reforming of CH_4 : mol.m^{-3}.s^{-1}
(c)
T (K) SOFC; Potential: 0.5V
Interconnector
Air Channel
Electrolyte
Porous Cathode
(d)

Figure 4

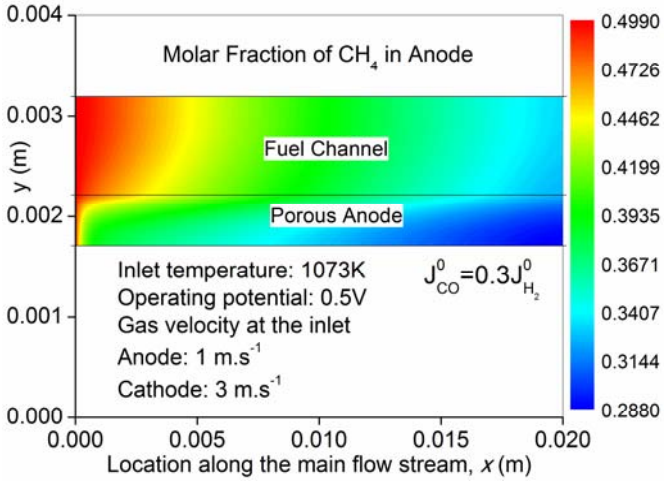
Molar Fraction of CH_4 in Anode
Fuel Channel
Porous Anode
Inlet temperature: 1073K
Operating potential: 0.5V
Gas velocity at the inlet
Anode: 1 m.s^{-1}
Cathode: 3 m.s^{-1}
$J^0_{CO}=0.3J^0_{H_2}$
y (m)
Location along the main flow stream, x (m)
0.004
0.003
0.002
0.001
0.000
0.000
0.005
0.010
0.015
0.020
0.4990
0.4726
0.4462
0.4199
0.3935
0.3671
0.3407
0.3144
0.2880

(a)

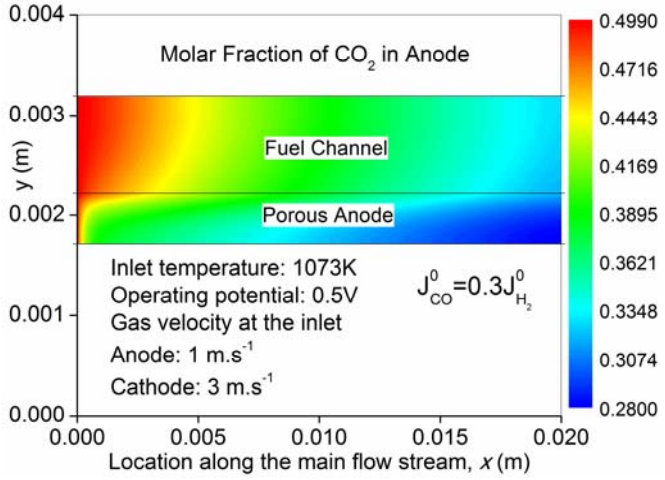
Molar Fraction of CO_2 in Anode
Fuel Channel
Porous Anode
Inlet temperature: 1073K
Operating potential: 0.5V
Gas velocity at the inlet
Anode: 1 m.s^{-1}
Cathode: 3 m.s^{-1}
$J^0_{CO}=0.3J^0_{H_2}$
y (m)
Location along the main flow stream, x (m)
0.004
0.003
0.002
0.001
0.000
0.000
0.005
0.010
0.015
0.020
0.4990
0.4716
0.4443
0.4169
0.3895
0.3621
0.3348
0.3074
0.2800

(b)

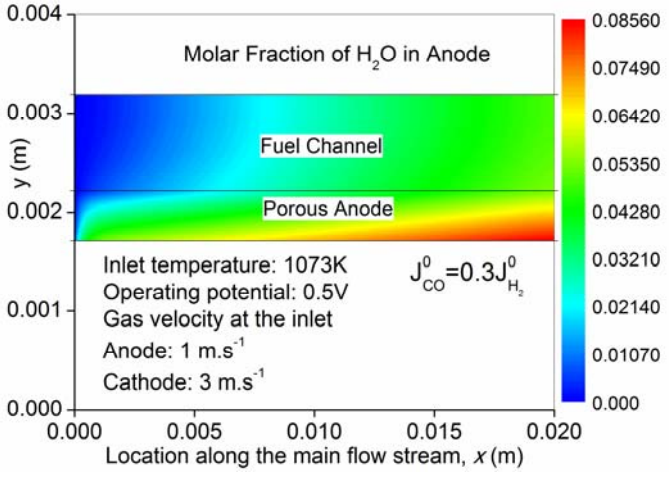
Molar Fraction of H_2O in Anode
Fuel Channel
Porous Anode
Inlet temperature: 1073K
Operating potential: 0.5V
Gas velocity at the inlet
Anode: 1 m.s^{-1}
Cathode: 3 m.s^{-1}
$J^0_{CO}=0.3J^0_{H_2}$
y (m)
Location along the main flow stream, x (m)
0.004
0.003
0.002
0.001
0.000
0.000
0.005
0.010
0.015
0.020
0.08560
0.07490
0.06420
0.05350
0.04280
0.03210
0.02140
0.01070
0.000

(c)

Figure 5

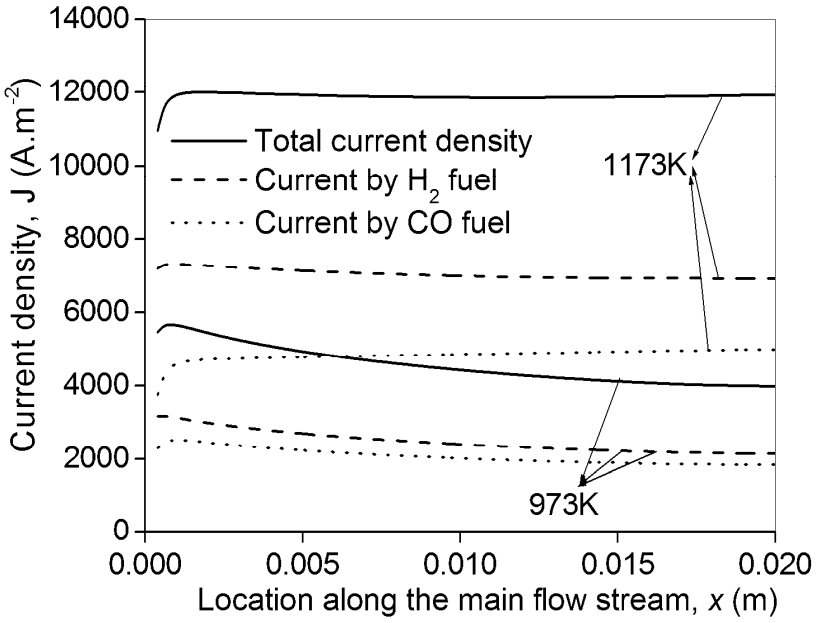
14000
12000
10000
8000
6000
4000
2000
0
Current density, J (A.m-2)
Total current density
Current by H2 fuel
Current by CO fuel
1173K
973K
0.000
0.005
0.010
0.015
0.020
Location along the main flow stream, x (m)

Figure 6

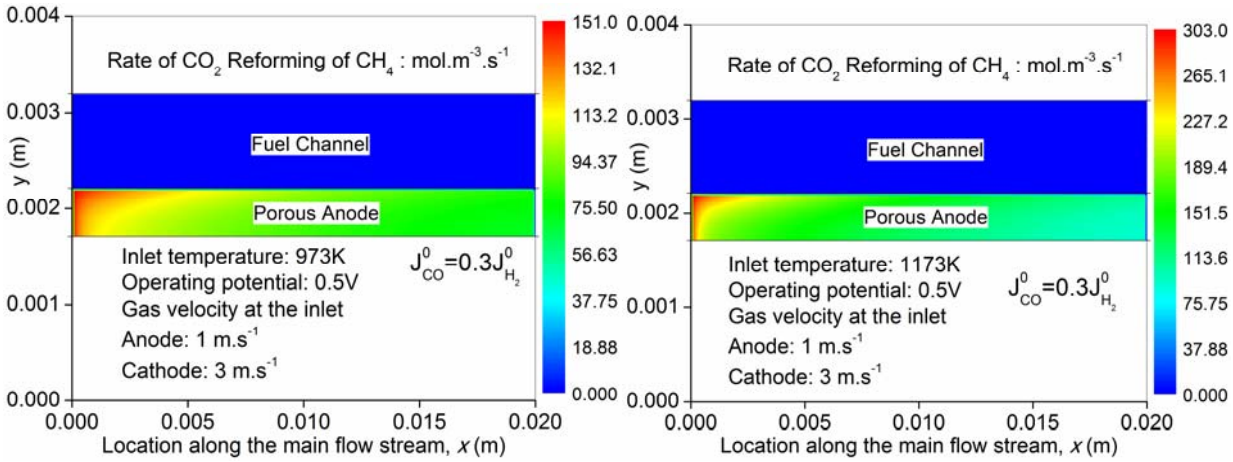
Rate of CO_2 Reforming of CH_4 : mol.m^{-3}.s^{-1}
Fuel Channel
Porous Anode
Inlet temperature: 973K
Operating potential: 0.5V
Gas velocity at the inlet
Anode: 1 m.s^{-1}
Cathode: 3 m.s^{-1}
$J^0_{CO}=0.3J^0_{H_2}$
y (m)
Location along the main flow stream, x (m)
151.0
132.1
113.2
94.37
75.50
56.63
37.75
18.88
0.000
Rate of CO_2 Reforming of CH_4 : mol.m^{-3}.s^{-1}
Fuel Channel
Porous Anode
Inlet temperature: 1173K
Operating potential: 0.5V
Gas velocity at the inlet
Anode: 1 m.s^{-1}
Cathode: 3 m.s^{-1}
$J^0_{CO}=0.3J^0_{H_2}$
303.0
265.1
227.2
189.4
151.5
113.6
75.75
37.88
0.000

(a) (b)

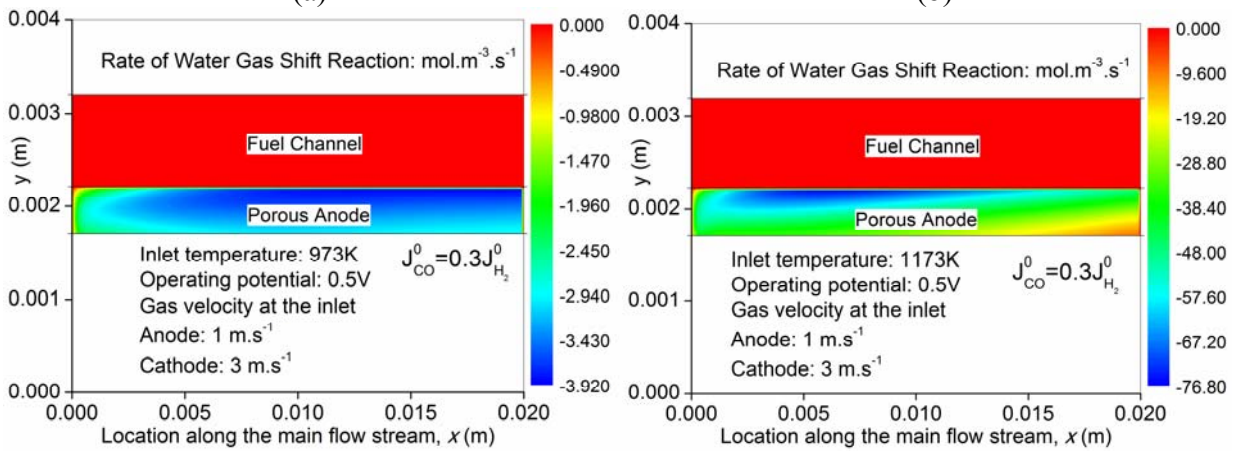
Rate of Water Gas Shift Reaction: mol.m^{-3}.s^{-1}
Fuel Channel
Porous Anode
Inlet temperature: 973K
Operating potential: 0.5V
Gas velocity at the inlet
Anode: 1 m.s^{-1}
Cathode: 3 m.s^{-1}
$J^0_{CO}=0.3J^0_{H_2}$
y (m)
Location along the main flow stream, x (m)
0.000
-0.4900
-0.9800
-1.470
-1.960
-2.450
-2.940
-3.430
-3.920
Rate of Water Gas Shift Reaction: mol.m^{-3}.s^{-1}
Fuel Channel
Porous Anode
Inlet temperature: 1173K
Operating potential: 0.5V
Gas velocity at the inlet
Anode: 1 m.s^{-1}
Cathode: 3 m.s^{-1}
$J^0_{CO}=0.3J^0_{H_2}$
0.000
-9.600
-19.20
-28.80
-38.40
-48.00
-57.60
-67.20
-76.80

(c) (d)

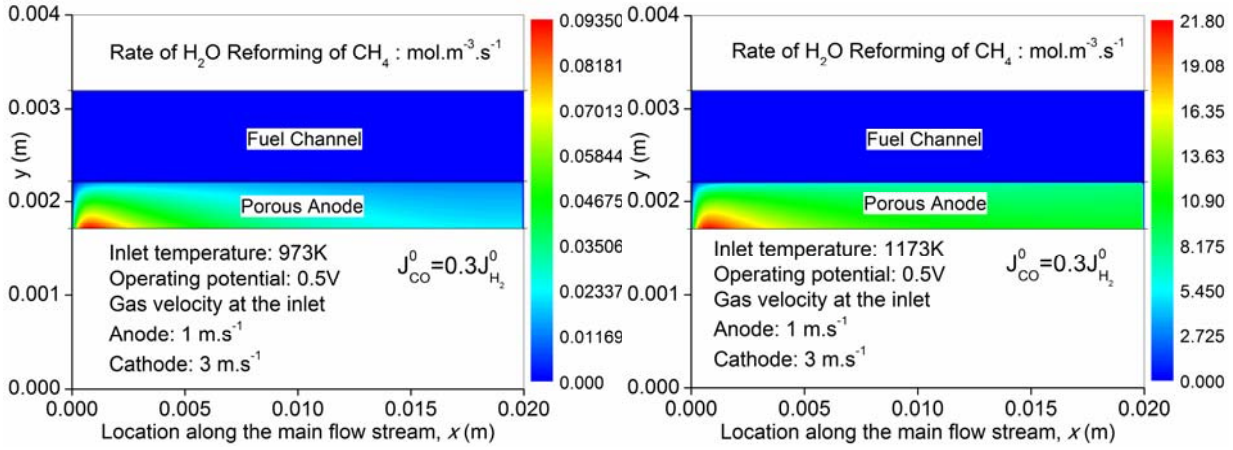
Rate of H_2O Reforming of CH_4 : mol.m^{-3}.s^{-1}
Fuel Channel
Porous Anode
Inlet temperature: 973K
Operating potential: 0.5V
Gas velocity at the inlet
Anode: 1 m.s^{-1}
Cathode: 3 m.s^{-1}
$J^0_{CO}=0.3J^0_{H_2}$
y (m)
Location along the main flow stream, x (m)
0.09350
0.08181
0.07013
0.05844
0.04675
0.03506
0.02337
0.01169
0.000
Rate of H_2O Reforming of CH_4 : mol.m^{-3}.s^{-1}
Fuel Channel
Porous Anode
Inlet temperature: 1173K
Operating potential: 0.5V
Gas velocity at the inlet
Anode: 1 m.s^{-1}
Cathode: 3 m.s^{-1}
$J^0_{CO}=0.3J^0_{H_2}$
21.80
19.08
16.35
13.63
10.90
8.175
5.450
2.725
0.000

(e) (f)

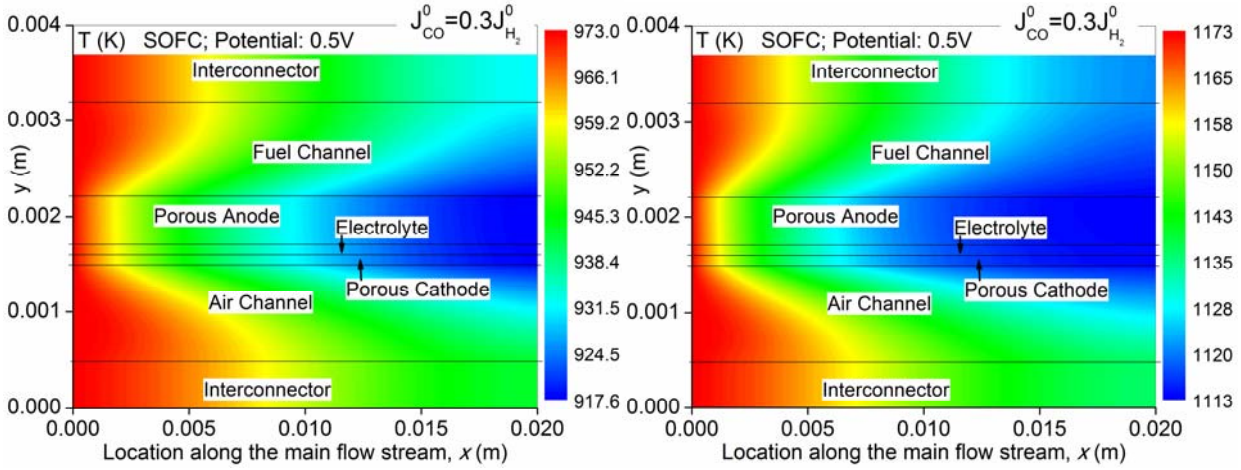
T (K) SOFC; Potential: 0.5V
$J^0_{CO}=0.3J^0_{H_2}$
Interconnector
Fuel Channel
Porous Anode
Electrolyte
Porous Cathode
Air Channel
Interconnector
y (m)
Location along the main flow stream, x (m)
0.000
0.005
0.010
0.015
0.020
0.001
0.002
0.003
0.004
973.0
966.1
959.2
952.2
945.3
938.4
931.5
924.5
917.6
1173
1165
1158
1150
1143
1135
1128
1120
1113

(g) (h)

Figure 7

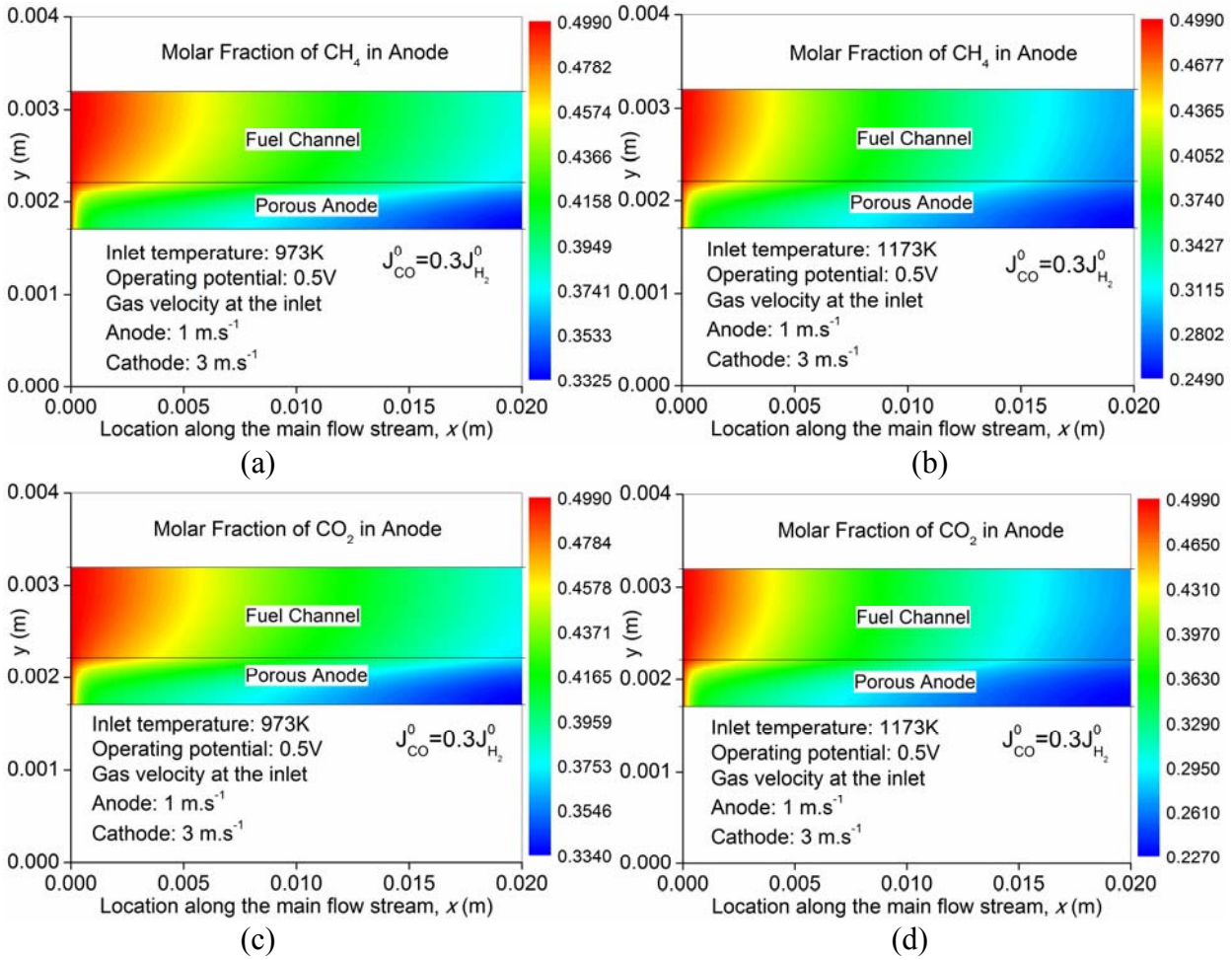
Molar Fraction of CH4 in Anode
Fuel Channel
Porous Anode
Inlet temperature: 973K
Operating potential: 0.5V
Gas velocity at the inlet
Anode: 1 m.s-1
Cathode: 3 m.s-1
J0CO=0.3J0H2
y (m)
Location along the main flow stream, x (m)
(a)
Molar Fraction of CH4 in Anode
Fuel Channel
Porous Anode
Inlet temperature: 1173K
Operating potential: 0.5V
Gas velocity at the inlet
Anode: 1 m.s-1
Cathode: 3 m.s-1
J0CO=0.3J0H2
y (m)
Location along the main flow stream, x (m)
(b)
Molar Fraction of CO2 in Anode
Fuel Channel
Porous Anode
Inlet temperature: 973K
Operating potential: 0.5V
Gas velocity at the inlet
Anode: 1 m.s-1
Cathode: 3 m.s-1
J0CO=0.3J0H2
y (m)
Location along the main flow stream, x (m)
(c)
Molar Fraction of CO2 in Anode
Fuel Channel
Porous Anode
Inlet temperature: 1173K
Operating potential: 0.5V
Gas velocity at the inlet
Anode: 1 m.s-1
Cathode: 3 m.s-1
J0CO=0.3J0H2
y (m)
Location along the main flow stream, x (m)
(d)

Figure 8

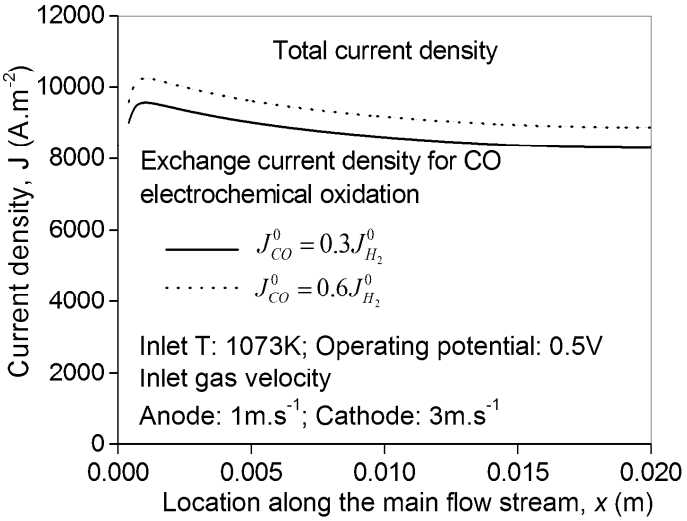
Total current density
Exchange current density for CO electrochemical oxidation
$J^0_{CO} = 0.3J^0_{H_2}$
$J^0_{CO} = 0.6J^0_{H_2}$
Inlet T: 1073K; Operating potential: 0.5V
Inlet gas velocity
Anode: 1m.s^{-1}; Cathode: 3m.s^{-1}
Current density, J (A.m^{-2})
Location along the main flow stream, x (m)

(a)

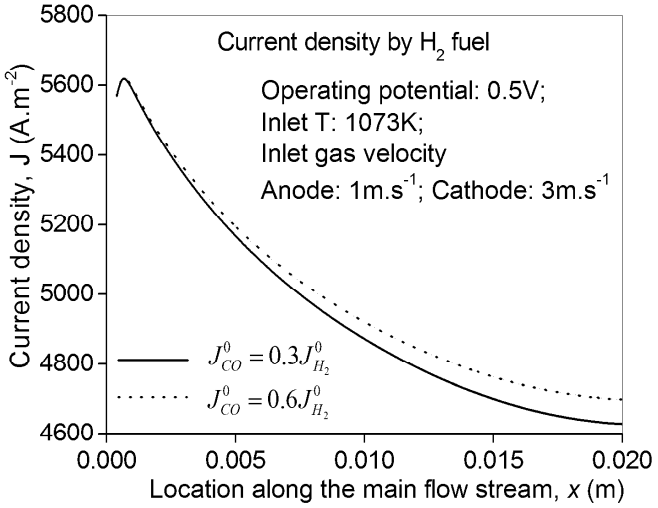
Current density by H_2 fuel
Operating potential: 0.5V;
Inlet T: 1073K;
Inlet gas velocity
Anode: 1m.s^{-1}; Cathode: 3m.s^{-1}
$J^0_{CO} = 0.3J^0_{H_2}$
$J^0_{CO} = 0.6J^0_{H_2}$
Current density, J (A.m^{-2})
Location along the main flow stream, x (m)

(b)

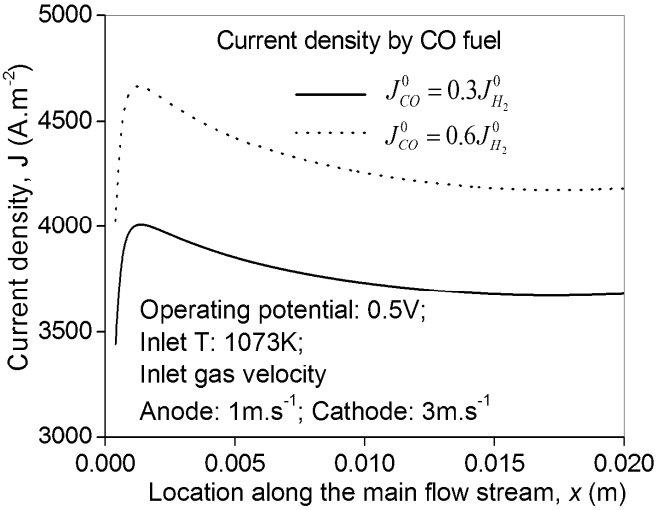
Current density by CO fuel
$J^0_{CO} = 0.3J^0_{H_2}$
$J^0_{CO} = 0.6J^0_{H_2}$
Operating potential: 0.5V;
Inlet T: 1073K;
Inlet gas velocity
Anode: 1m.s^{-1}; Cathode: 3m.s^{-1}
Current density, J (A.m^{-2})
Location along the main flow stream, x (m)

(c)

Figure 9

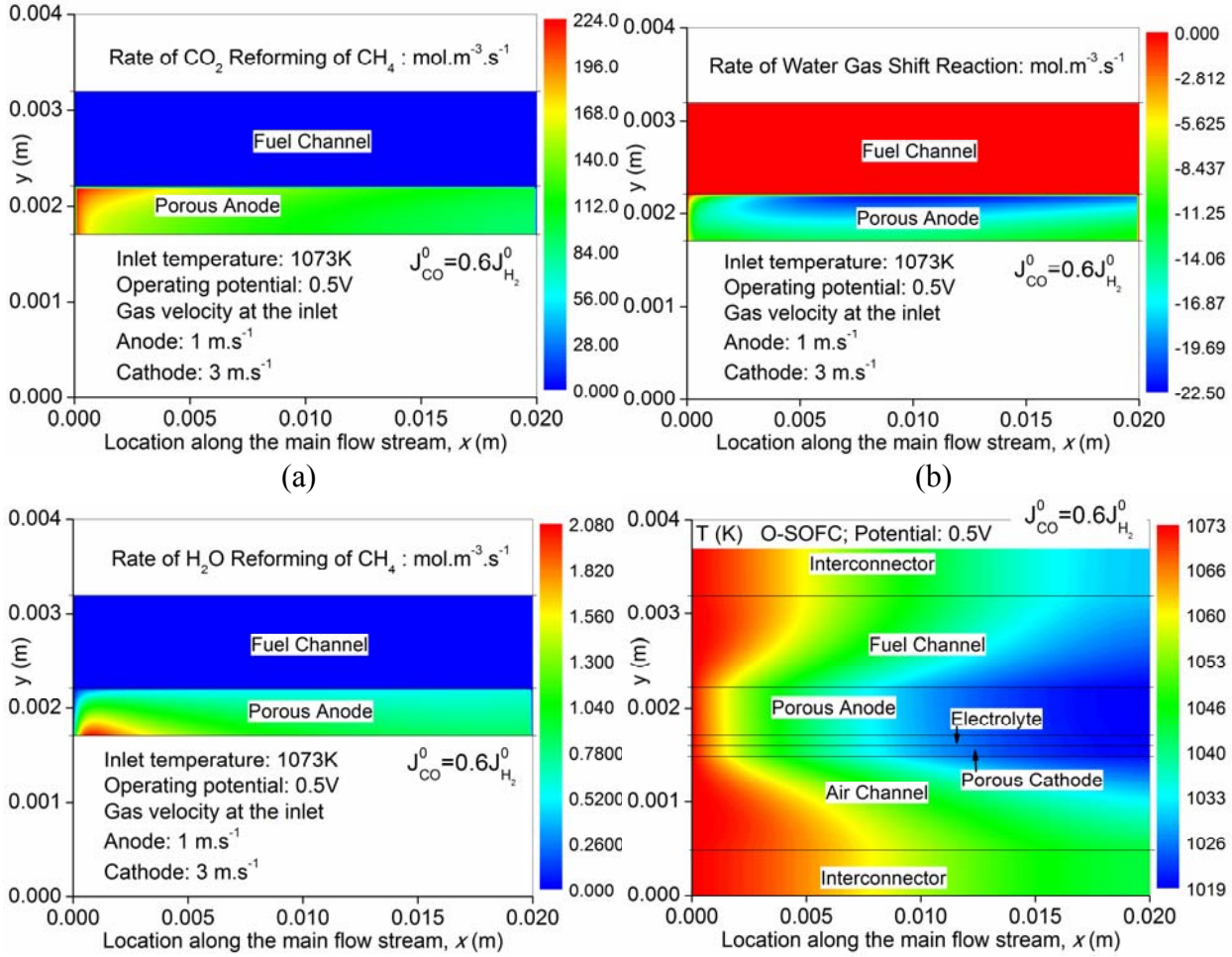
Rate of CO_2 Reforming of CH_4 : mol.m^{-3}.s^{-1}
Fuel Channel
Porous Anode
Inlet temperature: 1073K
Operating potential: 0.5V
Gas velocity at the inlet
Anode: 1 m.s^{-1}
Cathode: 3 m.s^{-1}
$J^0_{CO}=0.6J^0_{H_2}$
y (m)
Location along the main flow stream, x (m)
(a)
Rate of Water Gas Shift Reaction: mol.m^{-3}.s^{-1}
Fuel Channel
Porous Anode
Inlet temperature: 1073K
Operating potential: 0.5V
Gas velocity at the inlet
Anode: 1 m.s^{-1}
Cathode: 3 m.s^{-1}
$J^0_{CO}=0.6J^0_{H_2}$
y (m)
Location along the main flow stream, x (m)
(b)
Rate of H_2O Reforming of CH_4 : mol.m^{-3}.s^{-1}
Fuel Channel
Porous Anode
Inlet temperature: 1073K
Operating potential: 0.5V
Gas velocity at the inlet
Anode: 1 m.s^{-1}
Cathode: 3 m.s^{-1}
$J^0_{CO}=0.6J^0_{H_2}$
y (m)
Location along the main flow stream, x (m)
(c)
T (K) O-SOFC; Potential: 0.5V
$J^0_{CO}=0.6J^0_{H_2}$
Interconnector
Fuel Channel
Porous Anode
Electrolyte
Air Channel
Porous Cathode
Interconnector
y (m)
Location along the main flow stream, x (m)
(d)

Figure 10

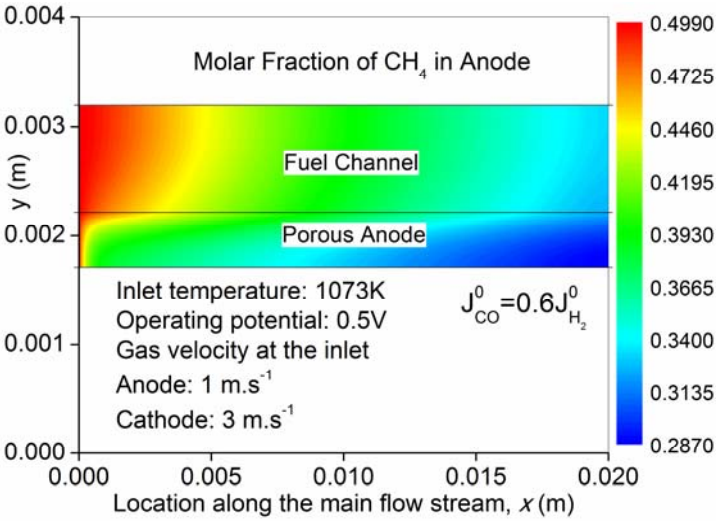

(a)

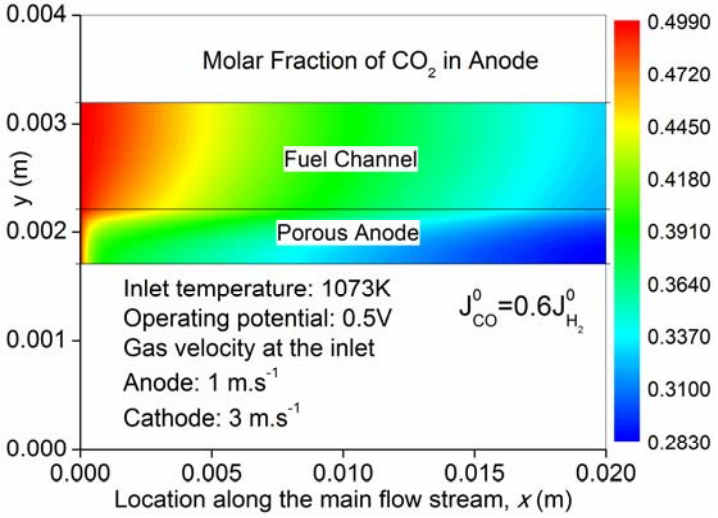

(b)

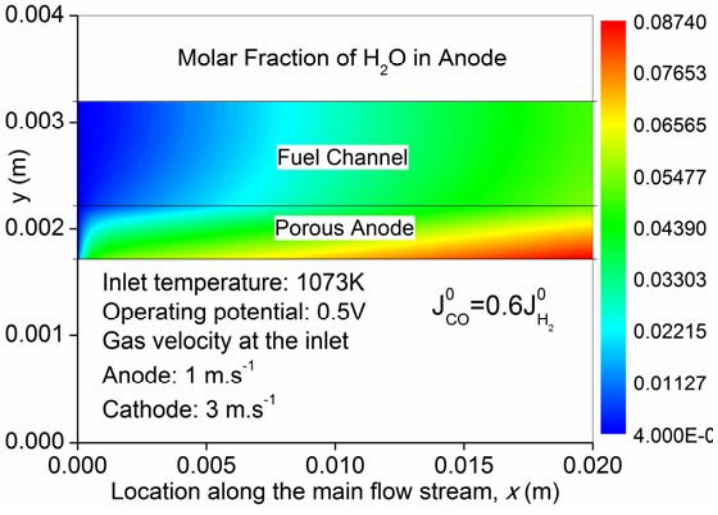

(c)

Figure 11

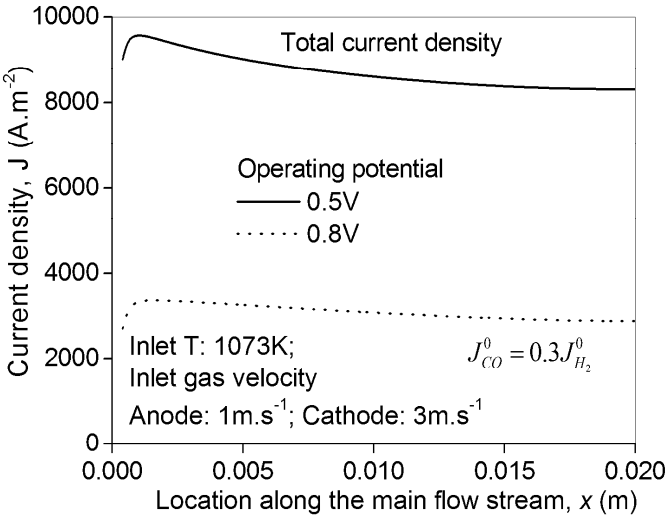

(a)

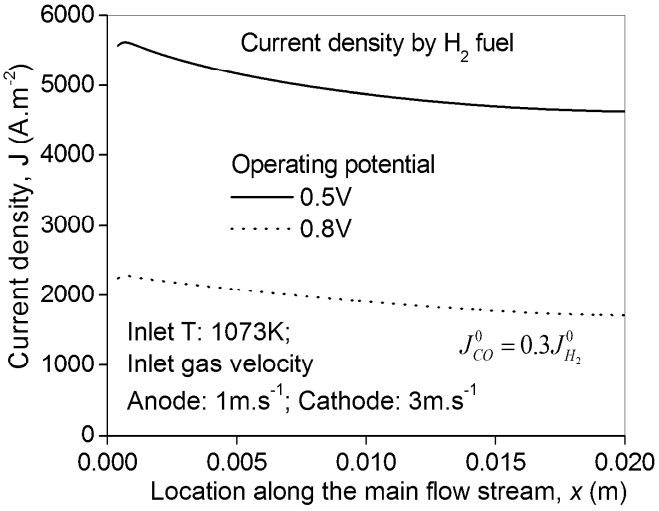

(b)

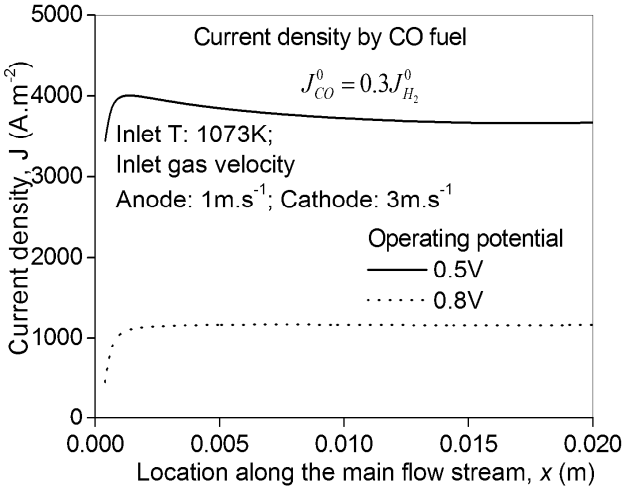

(c)

Figure 12

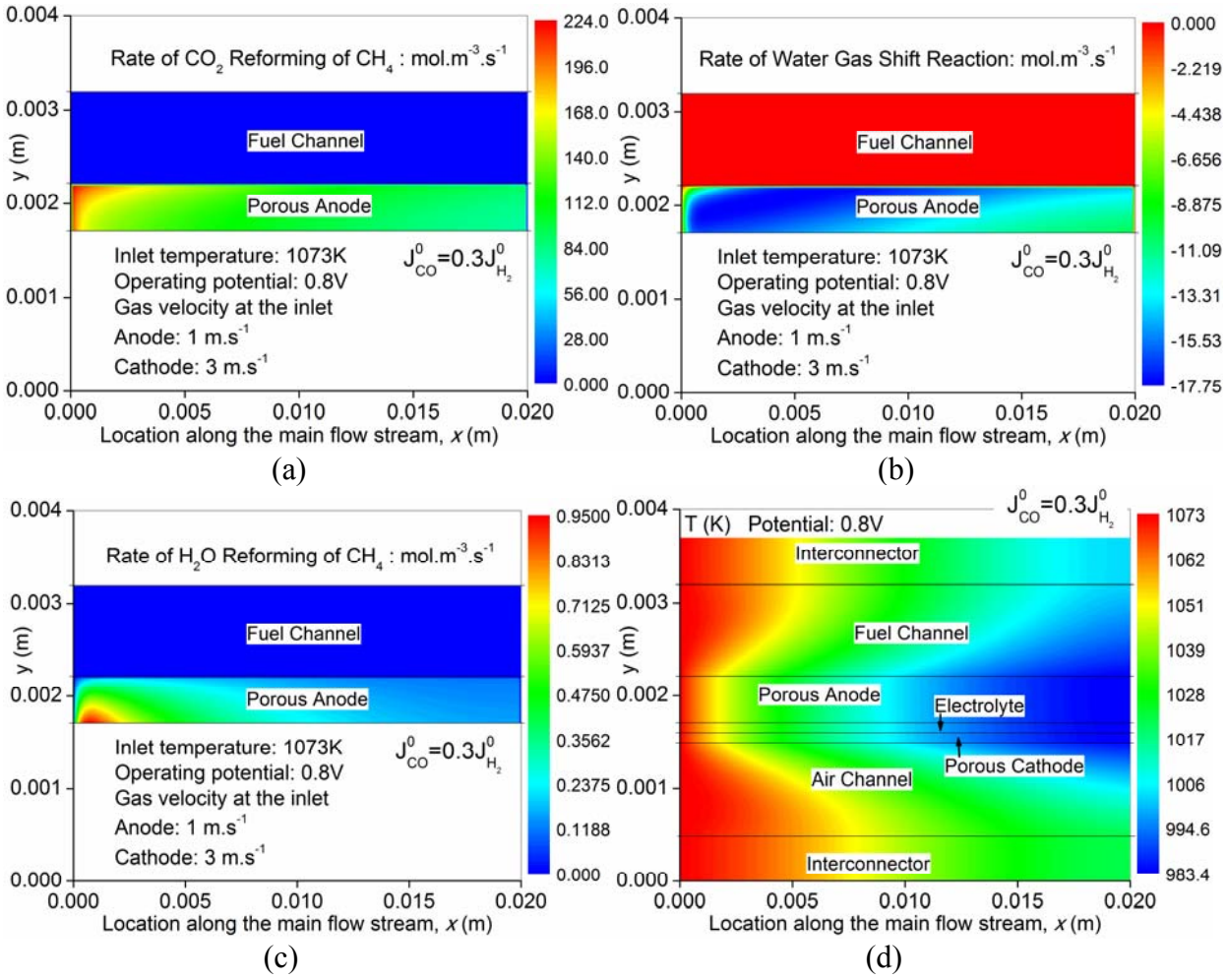
Rate of CO_2 Reforming of CH_4 : mol.m^{-3}.s^{-1}
Fuel Channel
Porous Anode
Inlet temperature: 1073K
Operating potential: 0.8V
Gas velocity at the inlet
Anode: 1 m.s^{-1}
Cathode: 3 m.s^{-1}
$J^0_{CO}=0.3J^0_{H_2}$
y (m)
Location along the main flow stream, x (m)
(a)
Rate of Water Gas Shift Reaction: mol.m^{-3}.s^{-1}
(b)
Rate of H_2O Reforming of CH_4 : mol.m^{-3}.s^{-1}
(c)
T (K) Potential: 0.8V
Interconnector
Electrolyte
Porous Cathode
Air Channel
(d)

Figure 13

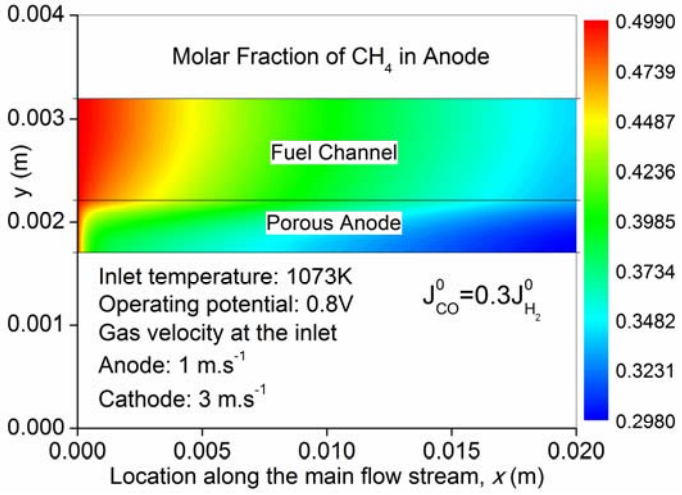

(a)

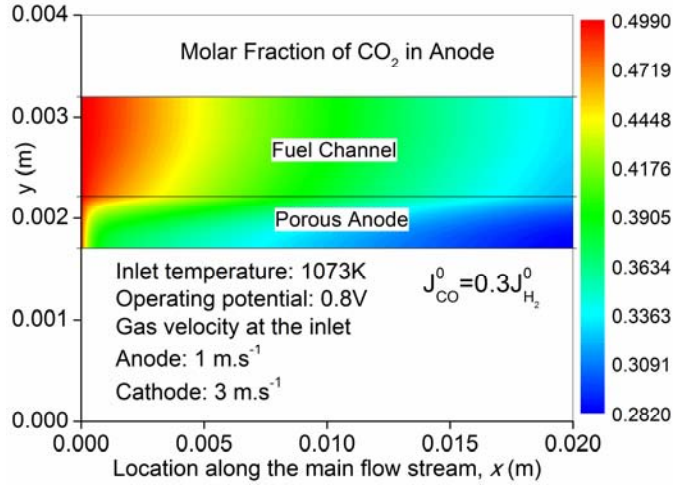

(b)

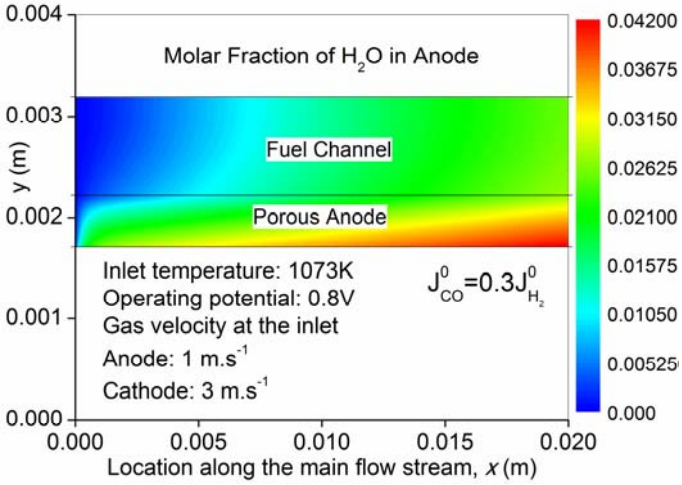

(c)

Figure 14